Implementation and validation of a total displacement non-linear homogenization approach for in-plane loaded masonry

by

Elisa Bertolesi[(1)], Gabriele Milani[(1)*], Paulo B Lourenço[(2)]

(1) Department of Architecture, Built environment and Construction engineering ABC Politecnico di Milano, Piazza Leonardo da Vinci 32, 20133 Milan, Italy

(2) ISISE, Department of Civil Engineering, University of Minho, Guimarães Portugal

* Corresponding author. E-mail: gabriele.milani@polimi.it. Phone: +39 022399 4225 Fax: +39 022399 4220

Keywords: *Masonry; in-plane loads; semi-analytical approach; compatible model of homogenization; holonomic non-linear model.*

Abstract

Two simple homogenization models suitable for the non-linear analysis of masonry walls in-plane loaded are presented. A rectangular running bond elementary cell is discretized by means of twenty-four constant stress three-noded plane-stress triangular elements and linear two-noded interfaces. Non-linearity is concentrated on mortar reduced to interface, exhibiting a holonomic behavior with softening. The paper shows how the mechanical problem in the unit cell can be characterized by very few displacement/stress variables and how homogenized stress-strain behavior can be evaluated by means of a small-scale system of non-linear equations. At a structural level, it is therefore not necessary to solve a homogenization problem at each load step in each Gauss point and a direct implementation into commercial software as an external user supplied subroutine is straightforward. Non-linear structural analyses are conducted on a variety of different problems, for which experimental and numerical data are available in the literature, in order to show that accurate results can be obtained with a limited computational effort.

1. Introduction

Masonry is a composite material constituted by bricks (or blocks) joined by mortar. The variability of the masonry bond (or arrangement of the bricks), the shape and dimension of the bricks, as well as the quasi-fragile behavior of the constituent materials, make the simulation of masonry still a challenging task. At present, two main approaches are utilized to numerically describe masonry behavior after the elastic limit, which usually is exceeded at low levels of external loads, known in the technical literature as macro-modeling and micro-modeling.

Macro-modeling does not make any distinction between masonry units and joints, averaging the effect of mortar through the formulation of a fictitious continuous material. The literature in this regard is extensive [1]-[3], with the noticeable example of no-tension material modeling (e.g. [1]), traditionally conceived to deal with non-linear problems exhibiting predominant mode I fracture of the joints (e.g. arches or pillars under rocking) and masonry with good compressive strength, where crushing and orthotropic behavior are not paramount. Macro-modeling allows the rough discretizations necessary for the analysis of large scale structures. Nevertheless, it is difficult to take into account some distinctive aspects of masonry in this approach, such as anisotropy in the inelastic range and the post-peak softening behavior in both tension and compression, unless sophisticated approaches with multiple inelastic parameters are adopted. In this regard, some equivalent macro-models have been presented [2]-[3], featuring orthotropic elastic-plastic behavior with softening. Theoretically, such approaches are capable of adequately estimating the non-linear masonry behavior along any load combination, even if some limitations may occur in specific cases (see [4] for a detailed discussion). Costly experimental campaigns are needed to consistently evaluate data fitting mechanical coefficients that fully define the models.

The alternative micro-modeling approach is simply characterized by distinct modeling of mortar joints and bricks at structural level. The reduction of joints to interfaces [5]-[7] helps in limiting variables, especially in the non-linear range, but the approach is computationally demanding and the need of modeling separately bricks and mortar limits its applicability to structural elements and small case studies. Therefore, it can be stated that, at present, the analysis of masonry walls in the inelastic range requires macro-scale computations with finite elements (FEs) [8][9]. In such scenario, homogenization [10]-[19] is a fair compromise between micro- and macro-modeling, because it allows non-linear analyses of large scale structures, still considering the real disposition of bricks and the actual mechanical properties of the constituent materials at a cell level. Clearly, the numerical models to use at structural level should be sufficiently simple, reliable and efficient to allow a quick evaluation of (a) collapse loads, (b) displacements near collapse and (c) post peak behavior of the structures.

Homogenization (or related simplified approaches) consists in extracting a representative element of volume (RVE) that generates the whole structure by repetition, in solving a boundary value problem on the RVE and in substituting the assemblage of bricks and mortar at a structural level with a fictitious orthotropic equivalent

material. The most straightforward procedure is the utilization of FEs [13][20], assuming either elasto-plastic or damaging constitutive laws for units and mortar. Nevertheless, the so-called FE^2, i.e. a twofold discretization, the first for the unit cell and the second at structural level, proved to be still too demanding, since the field problem has to be solved numerically for each load step, in each Gauss point. Alternatively, in this paper, a simplified homogenization two-step model is used to analyze masonry walls in-plane loaded. In the first step, masonry is substituted with a macroscopic equivalent material through a so-called compatible identification, belonging to the wide family of the homogenization procedures. The unit cell is meshed by means of 24 triangular constant stress (CST) plane stress elements (bricks) and linear interfaces for mortar joints. Triangular elements are assumed linear elastic, whereas the mechanical response of the interface elements includes two dominant failure modes, namely cracking (mode I) and shear (mode II) or a combination of two (mixed mode). Such elements are equipped with a constitutive relationship referred to as "holonomic", since expressed in terms of normal and tangential tractions σ and τ as a path independent function of the normal and tangential relative displacements at the interface. Both a piecewise linear and an exponential law are implemented, formally identical to an improved version of the Xu-Needleman law and proposed in another context [21]-[23]. Such cohesive relationships are characterized by a post-peak softening branch, possibly with coupling between normal and shear relationships in the case of the improved Xu-Needleman model.

Two slightly different approaches are compared. The first (Model I) translates the mechanical problem into mathematics by means of a system of a few non-linear equations, which is solved with standard general purpose algorithms. The second (Model II) is a semi-analytical two variables procedure. Whilst semi-analytical homogenization is a method already known and used in periodic fiber-reinforced composites, see e.g. [24], this is one of the first applications for periodic masonry, that at the same time allows a rigorous conservation of anti-periodicity of the stress field and periodicity of displacements.

In the second step, entire masonry walls are analyzed in the inelastic range by means of a commercial FE code where the discretization is constituted by quadrilateral rigid elements and homogenized holonomic tensile-shear springs. It is worth mentioning that most commercial codes can be suitably used at this aim. The procedure is efficient and reliable because: (1) the disadvantages of FE^2 are superseded since the solution in terms of

displacements and stresses is found at a cell level with very limited computational effort, using an implementation of the routine adopted at a meso-level to evaluate homogenized quantities directly at structural level; (2) it is not necessary to discretize with refined meshes the elementary cell and hence Gauss point computations are much faster, where only few kinematic stress variables are needed; and (3) the holonomic laws assumed for mortar joint allow for a total displacement formulation of the model, where the only variables entering into the homogenization problem are represented by displacements.

2. The simplified (compatible homogenization) holonomic model

One of the basic concepts of homogenization relies in introducing averaged quantities representing the macroscopic strain and stress tensors (respectively $\mathbf{E}$ and $\mathbf{\Sigma}$) [13] [25] on a representative element of volume *Y* (RVE or elementary cell, Figure 1), i.e. $\mathbf{E} = <\boldsymbol{\varepsilon}> = \frac{1}{A}\int_Y \boldsymbol{\varepsilon}(\mathbf{u})dY$ and $\mathbf{\Sigma} = <\boldsymbol{\sigma}> = \frac{1}{A}\int_Y \boldsymbol{\sigma}dY$, where *A* stands for the area of the elementary cell, $\boldsymbol{\varepsilon}$ and $\boldsymbol{\sigma}$ stand for the local quantities (strains and stresses respectively) and <*> is the averaging operator. Periodicity conditions are imposed on the stress field $\boldsymbol{\sigma}$ and the displacement field **u**, given by:

$$\begin{cases} \mathbf{u} = \mathbf{E}\mathbf{y} + \mathbf{u}^{\text{per}} & \mathbf{u}^{\text{per}} \text{ on } \partial Y \\ \boldsymbol{\sigma}\mathbf{n} & \text{anti-periodic} \quad \text{on} \quad \partial Y \end{cases} \tag{1}$$

where $\mathbf{u}$ is the total displacement field, $\mathbf{u}^{\text{per}}$ stands for a periodic displacement field, $\tilde{x} = \{x \quad y \quad z\}$ is the local frame of reference (see Figure 1), **E** is the homogenized strain tensor and **n** is the outward versor of the ∂Y surface.

In the model proposed, which is a simplified homogenization hereby designated as “compatible identification” (as coined in [26], where additional details can be found), joints are reduced to interfaces with zero thickness and bricks are discretized by means of a coarse mesh constituted by three noded plane-stress elements, as schematically sketched in Figure 1. The choice of meshing 1/4 of the brick through at least 3 triangular elements is due to the need of reproducing the presence of shear stress in the bed joint (element 2 in Figure 1) in horizontal stretching.

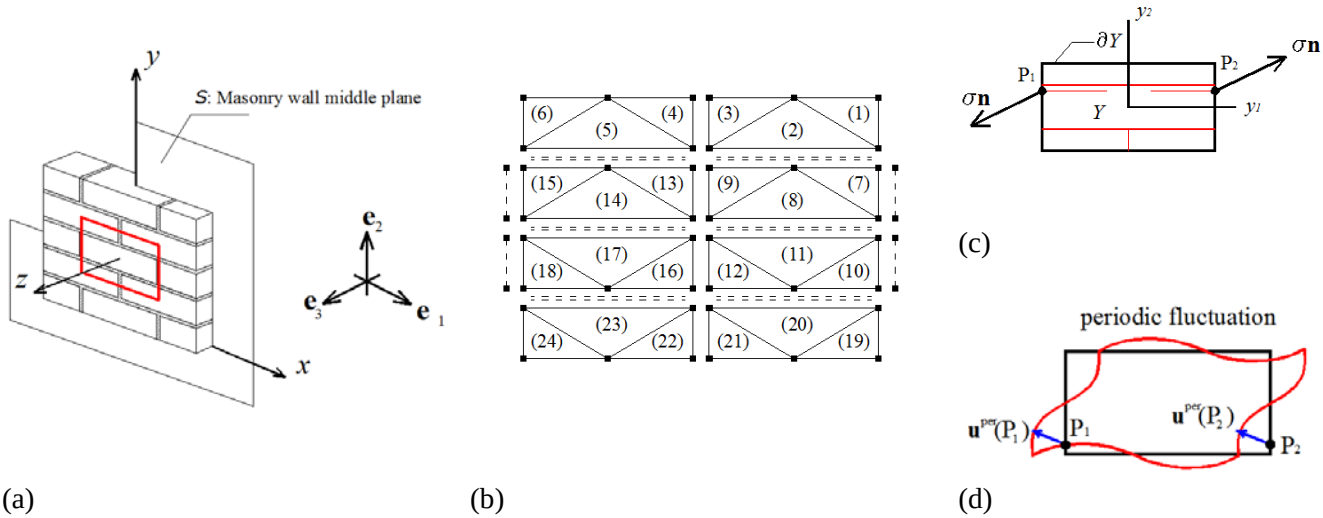

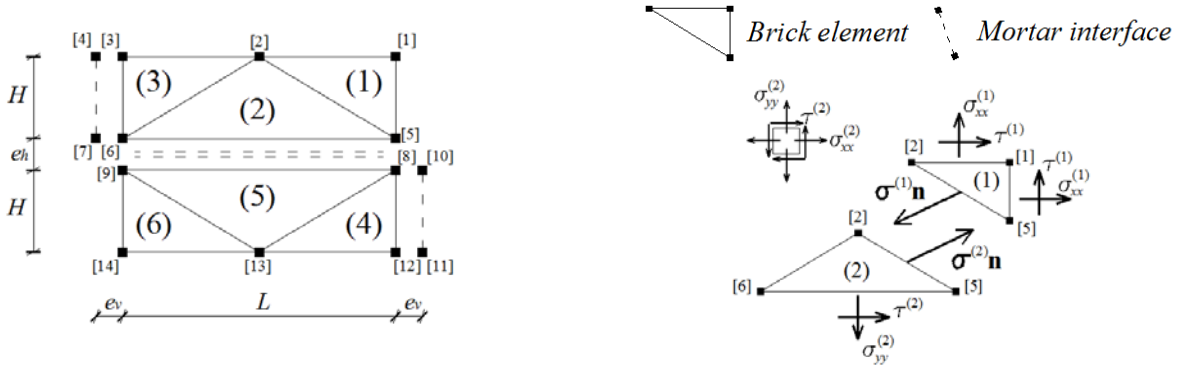

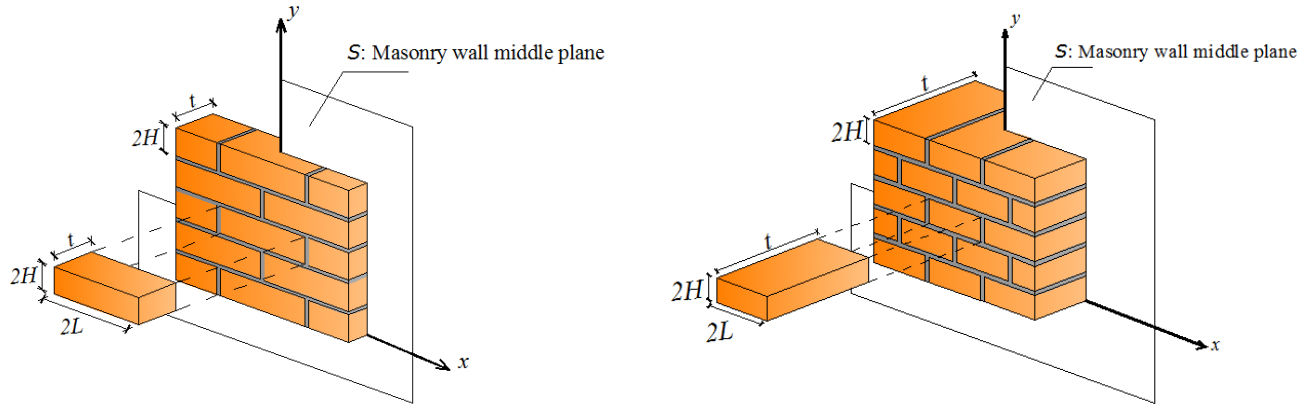

Figure 1: The micro-mechanical model proposed. –a and –b: subdivision of the RVE into 24 CST triangular elements (and 1/4 of the RVE into 6 elements). –c and –d: anti-periodicity of the micro-stress field and periodic displacement field. –e and –f: geometric properties of the cell, indication of nodes elements and element internal stresses. –g and –h: Type A and B masonry considered.

When dealing with the non-linear approach presented hereafter [11], all the non-linearity in the RVE is concentrated on joints reduced to interfaces. With the coarse discretization adopted, 1/4 of the RVE is meshed through 6 CST elements, labeled in Figure 1 as 1, 2, 3, 1', 2', 3'.

Indicating with $\circ^{(n)}$ a stress component belonging to the *n*-th element, the plane stress Cauchy stress tensor inside the *n*-th CST element $\boldsymbol{\sigma}^{(n)}$ is constituted by the components $\sigma_{xx}^{(n)}$ (horizontal stress), $\sigma_{yy}^{(n)}$ (vertical stress) and $\tau^{(n)}$ (shear stress). When dealing with static quantities, equilibrium inside each element is a-priori satisfied, $div\boldsymbol{\sigma} = 0$, whereas two equality constraints involving Cauchy stress tensor components of triangles have to be imposed for each internal interface between adjoining elements. In particular, for 1-2 interface, it has to be ensured that the stress vector (normal and tangential component) is equal passing from element 1 to element 2, i.e. $\sigma_{xx}^{(2)} = \sigma_{xx}^{(1)} + \rho\left(\tau^{(1)} - \tau^{(2)}\right)$ and $\sigma_{yy}^{(2)} = \sigma_{yy}^{(1)} + \rho^{-1}\left(\tau^{(1)} - \tau^{(2)}\right)$, where ρ is the ratio between the semi-length of the bricks and its height, i.e. $\rho = L/2H$. Analogous equations can be written for 3-2, 3'-2', 2-2' and 2'-1' interfaces.

Assuming that the triangular elements are linear elastic, the following relationship between strains and stresses can be written:

$$\begin{bmatrix} \varepsilon_{xx} \\ \varepsilon_{yy} \\ \gamma_{xy} \end{bmatrix} = \begin{bmatrix} \dfrac{\sigma_{xx}}{E_b} - \dfrac{\nu_b \sigma_{yy}}{E_b} \\ -\dfrac{\nu_b \sigma_{xx}}{E_b} + \dfrac{\sigma_{yy}}{E_b} \\ \dfrac{\tau}{G_b} \end{bmatrix} \qquad (2)$$

Here, E_b, ν_b and G_b are the brick elastic modulus, Poisson's ration and shear modulus, respectively.

3. *Two simple homogenization models*

In case of linear elastic bricks and mortar joints reduced to interfaces with either linear or non-linear (total strain or holonomic) behavior and within the FE discretization shown in Figure 1, two simple models are derived and hereafter briefly described. Both compatible homogenization strategies are implemented in suitable routines into

Matlab [27] and then interfaced at a structural level with the commercial code Abaqus [28], as it will be shown below. When dealing with masonry non-linear behavior, it is worth mentioning that the proposed approach concentrates all non-linearities on mortar joints, whereas bricks are assumed behaving elastically. A macroscopic approach is adopted in compression, i.e. an equivalent stress-strain relationship of the masonry material is assumed as in [5]. This is a much used and much more robust numerical approach, even if experimental evidence is that masonry fails in compression due to complex mechanisms involving crushing of bricks. This failure cannot be well reproduced with 2D approaches but requires either enriched plane-stress/plane-strain [12][14] procedures or full 3D FEM.

The simplified compatible identification procedure proposed allows for a separate analysis of the elementary cell under biaxial macroscopic strain state and pure shear deformation, see Figure 2 and Figure 3.

3.1. Biaxial strain state, Model I

In Model I, under a biaxial macroscopic strain state, i.e. for given values of boundary uniform displacements imposed $\overline{U}_x = (L + 2e_v)E_{xx}$ and $\overline{U}_y = (e_h + 2H)E_{yy}$, it can be easily shown that variables entering into the compatible homogenization approach are: $U_x^{[2]}, U_x^{[3]}, U_y^{[5]}, U_y^{[6]}, \sigma_{xx}^{(1)}, \sigma_{yy}^{(1)}, \tau_{xy}^{(1)}, \sigma_{xx}^{(2)}, \sigma_{yy}^{(2)}, \tau_{xy}^{(2)}, \sigma_{xx}^{(3)}, \sigma_{yy}^{(3)}, \tau_{xy}^{(3)}$. Here, $U^{[i]}$ is the i-th node displacement and $\sigma^{(i)}$ the i-th element stress.

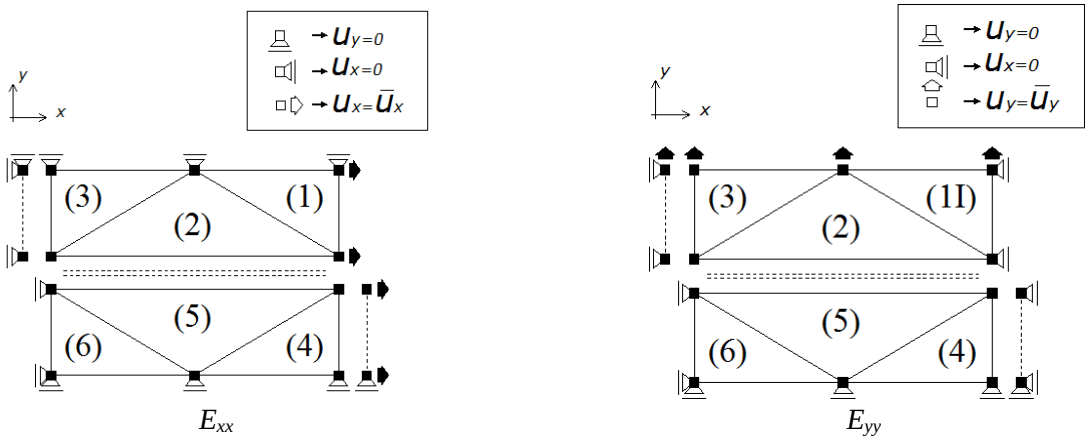

Figure 2: Boundary conditions applied in the models: tension along horizontal (a) and vertical (b) directions

Imposing equilibrium and compatibility on the unit cell, it can be easily shown that the following equations apply:

$$\sigma_{xx}^{(3)} = f_n^{\,I}\left(U_x^{[3]}\right) \quad \text{a} \qquad (1)$$

$$\tau_{xy}^{(3)} = 0 \quad \text{b}$$

$$\sigma_{yy}^{(2)} - \sigma_{yy}^{(3)} - \frac{2H}{L}\cdot\tau_{xy}^{(2)} = 0 \quad \text{c}$$

$$\sigma_{xx}^{(3)} - \sigma_{xx}^{(2)} + \frac{L}{2H}\cdot\tau_{xy}^{(2)} = 0 \quad \text{d}$$

$$\sigma_{yy}^{(2)} = f_n^{\,II}\left(U_y^{[5]} + U_y^{[6]} - \overline{U}_y\right) \quad \text{e}$$

$$\tau_{xy}^{(2)} = f_t^{\,II}\left(U_x^{[3]}\right) \quad \text{f}$$

$$\sigma_{xx}^{(3)} - \sigma_{xx}^{(1)} + \frac{L}{H}\cdot\tau_{xy}^{(2)} = 0 \quad \text{g}$$

$$\sigma_{yy}^{(2)} - \sigma_{yy}^{(1)} + \frac{2H}{L}\cdot\tau_{xy}^{(2)} = 0 \quad \text{h}$$

$$\tau_{xy}^{(1)} = 0 \quad \text{i}$$

$$U_x^{[3]} + \frac{L}{2E_b}\cdot\sigma_{xx}^{(1)} - \frac{L\cdot\nu_b}{2E_b}\cdot\sigma_{yy}^{(1)} + \frac{L}{2E_b}\cdot\sigma_{xx}^{(3)} - \frac{L\cdot\nu_b}{2E_b}\cdot\sigma_{yy}^{(3)} = 0 \quad \text{l}$$

$$U_y^{[5]} - \frac{H\cdot\nu_b}{E_b}\cdot\sigma_{xx}^{(1)} + \frac{H}{E_b}\cdot\sigma_{yy}^{(1)} = 0 \quad \text{m}$$

$$U_y^{[6]} - \frac{H\cdot\nu_b}{E_b}\cdot\sigma_{xx}^{(3)} + \frac{H}{E_b}\cdot\sigma_{yy}^{(3)} = 0 \quad \text{n}$$

$$U_x^{[2]} - \frac{L\cdot\nu_b}{2E_b}\cdot\sigma_{yy}^{(1)} + \frac{L}{2E_b}\cdot\sigma_{xx}^{(1)} = 0 \quad \text{o}$$

Here, the superscript "()" refers to the elements, "[]" to the nodes, and $f_n^{\,I}$, $f_t^{\,I}$, $f_n^{\,II}$, $f_t^{\,II}$ are respectively the non-linear normal and tangential laws implemented into the models in order to describe the behavior of the head and bed joints (I: head joint, II: bed joint).

Under a biaxial strain state, these equations represent a system of thirteen equations. In presence of linear elastic interfaces, the problem becomes trivial and can be easily solved without computational difficulties, but for non-linear interfaces, it is necessary to adopt an iterative procedure. In this case, the system can be formulated as a set of *n* non-linear equations in the form $F_i(x)$, with the aim of finding *x* so that $F_i(x)=0$. In order to find the unknowns and solve the set of equations, the aforementioned expressions have been implemented in Matlab [27]. The solver used, already implemented, works on an objective function to be minimized, which is the sum of squares of the

components $F_i(x)$. The residual at the converged solution must approximate zero and a starting vector of initial points provided by the user is needed. The algorithm used is a "trust-region reflective" and the basic idea is that the solver tries to approximate the function with a simpler one, typically quadratic, which behaves in a similar way to the original one in a given interval of points around *x* (the trust region). During the iterations, the solution vector of the previous iteration is used as the starting point for the following step. In order to improve the convergence of the algorithm, the Jacobian matrix is obtained explicitly. The aforementioned solver was used to solve both the piecewise linear and the Xu-Needleman exponential laws, adopted for the inelastic behavior.

3.2. Biaxial strain state, Model II

In the second model, it has been shown in [29] that independent variables are represented by displacements $\xi = \overline{U}_x^0 - U_x^9$ and $\eta = U_y^{[5]} + U_y^{[6]}$. They can be determined graphically plotting the following curves:

$$\text{Curve I: } \eta = \overline{U}_y^0 + \frac{2H}{\nu_b L}\left[\overline{U}_x^0 - \xi - L\frac{1-\nu_b^2}{E_b} f_n^I(\xi) - \frac{L^2}{2H}\frac{1-\nu_b^2}{E_b} f_t^{II}(\xi)\right]$$

$$\text{Curve II: } \xi = \overline{U}_x^0 + \frac{L}{2\nu_b H}\left[\overline{U}_y^0 - \eta - 2\frac{1-\nu_b^2}{E_b} H f_n^{II}(\eta)\right] \qquad (3)$$

The solution strategy is fully explained in [29], where the reader is referred to for further details. The determination of ξ and η allows for an evaluation of all static and kinematic internal variables and, hence, to homogenized stress quantities.

3.3. Shear deformation, Model I

Considering a pure shear deformation, the boundary uniform displacements applied are equal to $\overline{U}_x = (2H + e_h)E_{xy}$ and $\overline{U}_y = (L + 2e_v)E_{yx}$ as shown in Figure 3.

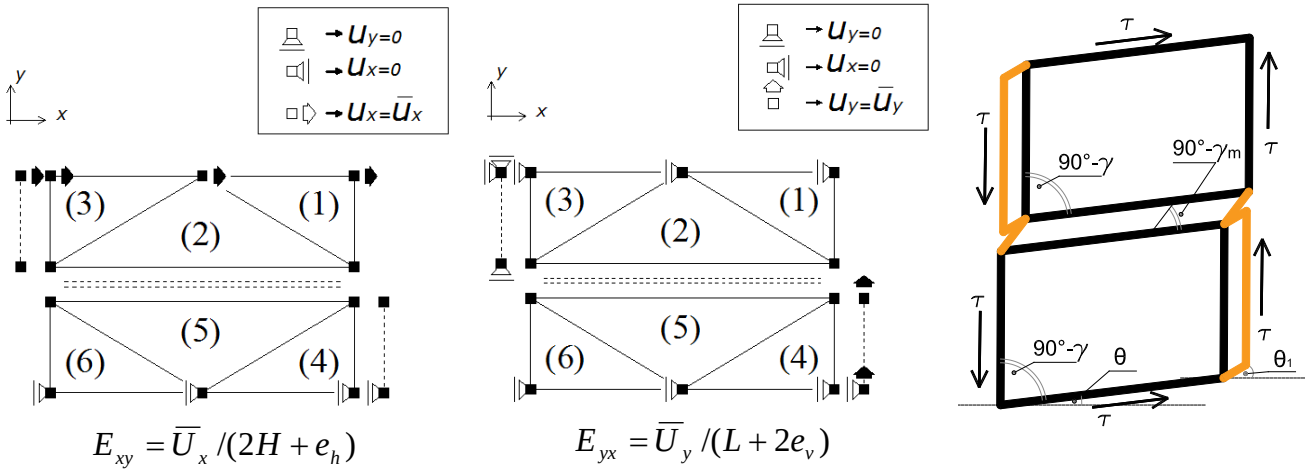

$$E_{xy} = \bar{U}_x / (2H + e_h)$$

-a

$$E_{yx} = \bar{U}_y / (L + 2e_v)$$

-b

-c

Figure 3: –a and –b: boundary conditions applied in the models, tangential deformation modes, E_{xy} (-a) and E_{yx} (-b). –c: kinematic and stress variables involved in the shear problem, model I.

With reference to Figure 3-c, it can be easily shown that the shear deformation problem in the Model I is governed by the following equations:

$$\begin{aligned}
&(L + e_v)\cdot\theta + e_v\cdot\theta_1 = E_{yx}\cdot(L + 2e_v) && \text{a}\\
&G_b\cdot\gamma - \tau = 0 && \text{b}\\
&G_m\cdot\theta_1 - \tau = 0 && \text{c}\\
&\frac{2H\cdot G_m}{e_h}\cdot(\theta - \gamma) + \frac{G_m}{2}\cdot\gamma_m - \tau = 0 && \text{d}\\
&2H\cdot\gamma + e_h\cdot\gamma_m = E_{xy}\cdot(2H + e_v) && \text{e}
\end{aligned} \qquad (3)$$

Eqs. (3) is a system of five non-linear equations, and five unknowns (ϑ, ϑ_1, τ, γ, γ_m), where E_{xy} and E_{yx} are prescribed macroscopic tangential strains as in Figure 3-a and -b. The adopted solution strategy is identical to that adopted for the biaxial strain state, i.e. a reflective thrust region method is used.

3.4. Shear deformation, Model II

Again in [29], it has been shown that in case of shear deformation independent variables are ξ^t, η^t and κ where

$$\xi^t = 2\overline{U}_x^t - \frac{H}{G_b}\left[-\frac{\overline{U}_y^t - \eta^t}{L/2}G_b + 2f_t^I\left(\eta^t\right) - \frac{4H}{L}f_n^{II}\left(\eta^t - \kappa\right) + 2\frac{\kappa}{L}G_b\right]$$

$$\eta^t = \overline{U}_y^t - \frac{L}{2G_b}\left[2f_t^{II}\left(\xi^t - \overline{U}_x^t\right) - \frac{2\overline{U}_x^t - \xi^t}{H}G_b + 2\frac{\kappa}{L}G_b\right] \qquad (4)$$

$$\kappa = \frac{e_v}{G_b}\left[2f_t^{II}\left(\xi^t - \overline{U}_x^t\right) - f_t^I\left(\eta^t\right)\right]$$

3.5. Holonomic relationships for mortar joints reduced to interfaces

Under mixed-mode loading conditions, expected to occur in mortar joints, two interface relationships are considered next and comparatively assessed: (a) A multi-linear relationship, with normal and tangential responses independent on each other (decoupled approach), i.e. $\sigma(\Delta_n)$ and $\tau(\Delta_t)$. Although not fully realistic, this approach is straightforward and allows for an impressive stability and rapid convergence of the algorithms. As an alternative, the cohesive relationship can be modified to take into account the frictional behavior among bricks. In this case, the peak tangential stress $\tau_{\lim}$ is assumed to depend on the current stress level at the interface σ by a classic Mohr-Coulomb criterion, namely $\tau_{\lim} = -\sigma + c\tan\varphi$, where φ and c denotes the friction angle and the cohesion, respectively. This choice may be useful to describe frictional sliding among the bricks; (b) The second choice is an improved version of the Xu–Needleman exponential law [21]-[23][30], hereafter called simply "Xu-Needleman" for the sake of conciseness. In this law, the stress vector ***T*** at the interface is given by the following closed-form expression:

$$\begin{aligned}\sigma &= \frac{\phi_n}{\delta_n}\left(\frac{\Delta_n}{\delta_n}\right)e^{-\left(\frac{\Delta_t}{\delta_t}\right)^2}e^{-\frac{\Delta_n}{\delta_n}} \\ \tau &= 2\frac{\phi_t}{\delta_t}\left(\frac{\Delta_t}{\delta_t}\right)\left(1+\frac{\Delta_n}{\delta_n}\right)e^{-\left(\frac{\Delta_t}{\delta_t}\right)^2}e^{-\frac{\Delta_n}{\delta_n}}\end{aligned} \qquad (5)$$

Symbols ϕ_n and ϕ_t denote the work of separation under pure Mode I (i.e. when $\Delta_t = 0$) and Mode II (i.e. when $\Delta_n = 0$), respectively, while δ_n and δ_t indicate the relevant characteristic lengths. It is worth emphasizing that equations (5) imply a strongly coupled response: softening occurs for both tractions although the interface is being stressed along one direction only. In compression, the response of mortar joints is assumed to be linear elastic until the interpenetration constraint is activated.

One may argue if the utilization of a (modified) Xu-Needleman law is suitable to properly represent the non-linear behavior of mortar joints. As a matter of fact, Xu and Needleman family of non-linear interface laws is particularly suited for cohesive interfaces, whereas friction is not precisely accounted for. Since Xu and Needleman introduced their exponential cohesive zone law in 1992, several authors have however extended and altered it, see [30] for a review. Very recently Liu and co-workers [31] have proposed a modification of the Xu-Needleman relationship to properly take into account frictional effects. First, the friction is assumed to increase nonlinearly at the delamination interface when the tangential cohesive softening appears. Second, a non-associative plasticity model based on the Mohr–Coulomb frictional contact law is proposed, which includes a frictional slip criterion and a slip potential function.

Here, a modification of the Xu-Needleman law is utilized exclusively at a cell level with a twofold aim. First, the interest of the authors is to test model robustness in presence of strong coupling and smooth non-linearity. Second, the aforementioned cohesive law is used to benchmark the results obtained when for joints a multi-linear simplified model is utilized, which accounts for friction but in a non rigorous way (i.e. not deriving stress-displacement curves from a potential, but assuming a Mohr-Coulomb criterion ruling exclusively the dependence of peak cohesion on normal stresses through friction). On the other hand, coupling between shear and normal stresses may be, at least in principle, paramount only for the bed joint in either horizontal or bi-axial stretching. Authors experienced that, in absence of imposed pre-compression, the level of normal stress on bed joint in the RVE is rather moderate, and this justifies the utilization of a modified Xu-Needleman law. A different situation may occur at a structural level, where there are some zones where the level of compression may be so high that compression crushing occurs. In this latter case, however, only the multi-linear approach is utilized, to approximate more consistently the actual behavior of the joints.

4. Comparisons at a cell level

4.1. Linear elastic case, comparison with closed form approaches

The first series of analyses presented are carried out assuming that mortar joints behave elastically. In order to validate the reliability of the homogenized mechanical properties provided by the model, the linear elastic moduli found are compared with those obtained by existing closed form procedures available in the literature, namely a recently presented approach based on the so-called method of cells [32] and the classical so called "layered model", by Pande et al. [33]. It is only worth noting that there are many reliable approaches for the estimation of the homogenized moduli to compare with, see for instance [34]-[37]. However, the analyses performed here have the sole aim of roughly evaluating the reliability of the present model in the linear elastic range by means of a comparison with two classic approaches and a recent procedure that seems to provide extremely accurate results.

The so-called layered model is probably one of the first pioneering attempts to provide homogenized elastic moduli in closed form that appeared in the literature. Masonry is considered constituted by superimposed horizontal layers of bricks and mortar bed joints, neglecting head joints. The hypothesis of not considering head joints leads however to inaccurate results when large differences occurs in the elastic parameters, as for instance in the horizontal Young's modulus. The model proposed by Pande et al. [33] is known in the literature as a two-step homogenization, in which the strong assumption of neglecting the head joints is removed. In the first step, bricks and head joints are homogenized separately, obtaining an intermediate orthotropic continuum. Then, in the second step, such continuum is further homogenized with the bed joints. Relatively simple closed form expressions are deduced, which proved to be sufficiently accurate when differences in the Young's moduli of the masonry components are not extrem. The approach has however some disadvantages, the most important being the dependence of the results from the order of homogenization.

Recently, Taliercio [32] has proposed to study the homogenization problem in the elastic range by means of a so-called method of cells (MoC), where the RVE is subdivided into six rectangular sub-domains where a polynomial expression for the displacement field is a-priori provided. The determination of the elastic coefficients is quite straightforward and closed form expressions are deduced from the minimization of the elastic energy. In detail,

two sub-models have been presented, the first derived from the original MoC approach, while the second (MSe) is an improved version of MoC.

Next, an elementary cell constituted by bricks of dimensions of 250x55x120 mm^3 (Standard Italian clay brick) and mortar joints 10 mm thick is considered. The Young's modulus and Poisson's ratio of bricks are kept constant and equal to 20000 MPa and 0.2, respectively. Different values of the mortar Young's modulus are considered, varying the E_b / E_m ratio in a wide range of technical applicability (from 1 to 1000), for representing very weak mud mortars or damaged joints, in which the stiffness swiftly degrades and progresses to zero.

In Figure 4, the homogenized elastic moduli and Poisson's ratio obtained using the aforementioned approaches (normalized against brick moduli) are depicted and compared with the present models. As noted, a global satisfactory agreement is found in the predictions obtained, also in comparison with more sophisticated approaches (i.e. MoC and MSe). As expected by the authors, a very good agreement is obtained particularly on E_{yy} and G_{xy} moduli. In such cases, indeed, even for low values of the E_b / E_m ratio, excellent accuracy is found. Slightly less accurate results are found for E_{xx} and Poisson's ratio (well in range of technical acceptability), due to the utilization of small bricks, which provides a large ratio joint thickness vs. brick height), and the relatively rough discretization of the stress and strain fields adopted for the bricks.

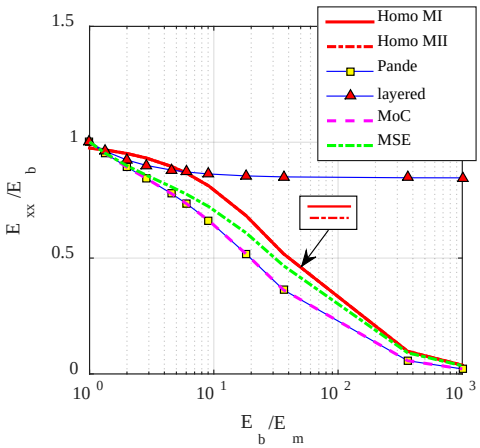

-a

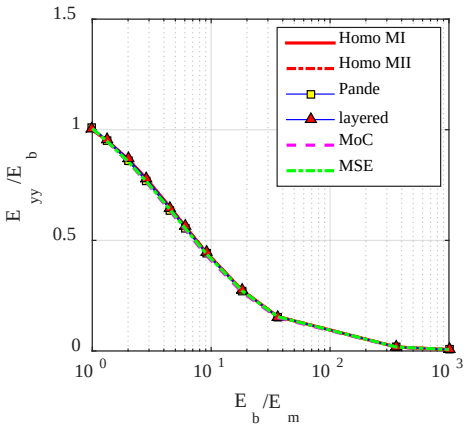

-b

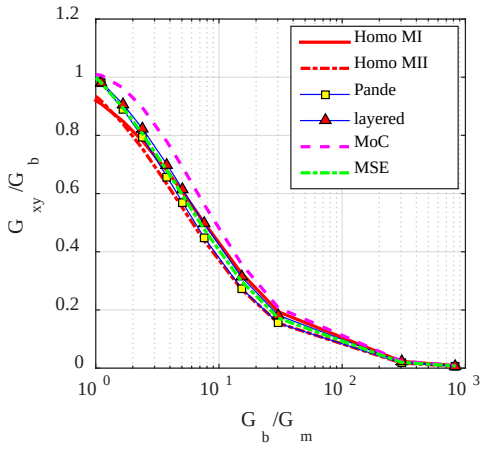

-c

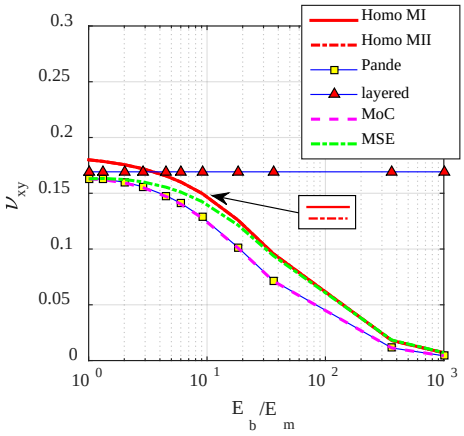

-d

Figure 4: Elastic parameters found at different E_b/E_m ratios. –a: E_{xx}. –b: E_{yy}. –c: G_{xy}. –d: ν_{xy}.

4.2. Nonlinear behavior

In the present section, the results obtained by the extension of the proposed approach to the non-linear range are discussed. In order to show the model capabilities, two masonry patterns commonly used in building practice are used, namely stretcher and header bonds, see Figure 1. In the following, we refer to the first case (Stretcher bond) with the label “Type A”, while “Type B” was used for the header bond masonry. For Type A, we consider bricks of dimensions equal to 122x37x54 mm^3 and mortar joints of thickness 5 mm, while for Type B, blocks of dimensions 250x55x120 mm^3 and mortar joints 10 mm thick are considered. As stated before, bricks are assumed to behave elastically, whereas mortar joints are reduced to interfaces obeying to nonlinear laws.

The mechanisms reproduced by the model are those involving joints failure, as expected. Cracking along joints represents one of the most common mechanisms occurring in practice, due to the low or negligible tensile strength that characterizes mortar bond. The elastic and inelastic mechanical properties used, for both the examples, are summarized in Tab. 1. For both patterns, Type A and B, two different holonomic non-linear laws for the description of the joint behavior have been adopted: the first one is a piecewise-linear law (labelled as PL), where only three mechanical parameters are needed (Young’s modulus, peak tensile stress and ultimate displacement). The second one is a Xu-Nedleman exponential law (labelled as XN), calibrated to obtain a behavior similar to the piecewise linear one. For the sake of clearness, the stress-jump of displacement laws adopted for head and bed joints, are depicted in Figure 5 and Figure 6.

		Mortar joints	***Bricks***
Stretcher bond model	Young's Modulus	E_m=1250 MPa	E_b=7000 MPa
	Poisson's ratio	-	ν=0.2
	Shear Modulus	G_m=0.4* E MPa	$G_b=E_b/[2(1+\nu)]$
	Peak tensile stress	f_t= 0.29 MPa	-
	Cohesion	c=1.4* f_t MPa	-
Header bond model	Young's Modulus	E_m=1500 MPa	E_b=8000 MPa
	Poisson's ratio	-	ν=0.2
	Shear Modulus	G_m=0.4* E MPa	$G_b=E_b/[2(1+\nu)]$
	Peak tensile stress	f_t= 0.1 MPa	-
	Cohesion	c=0.1 MPa	-

Tab. 1. Mechanical properties used for the constituent materials in the non-linear range.

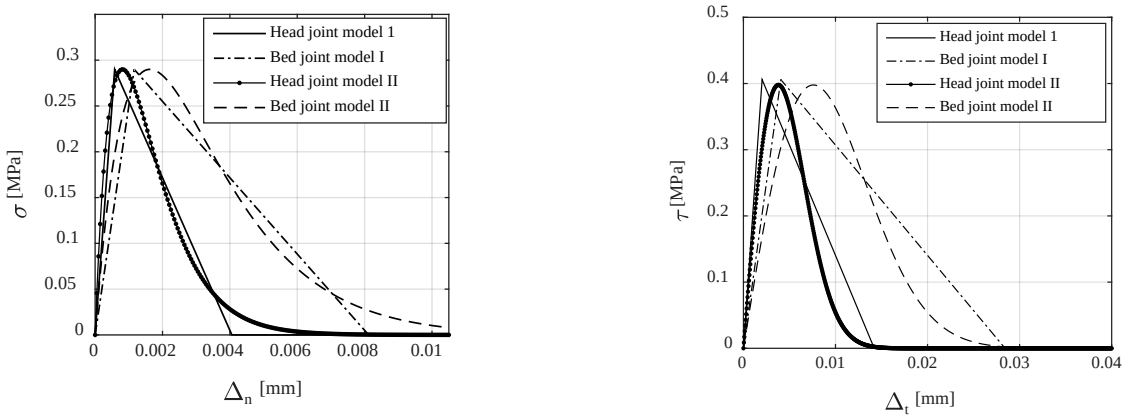

a b

Figure 5: Stress-jump of displacement curves adopted for the mortar joints interfaces (stretcher bond model): normal (a) and tangential (b) behavior.

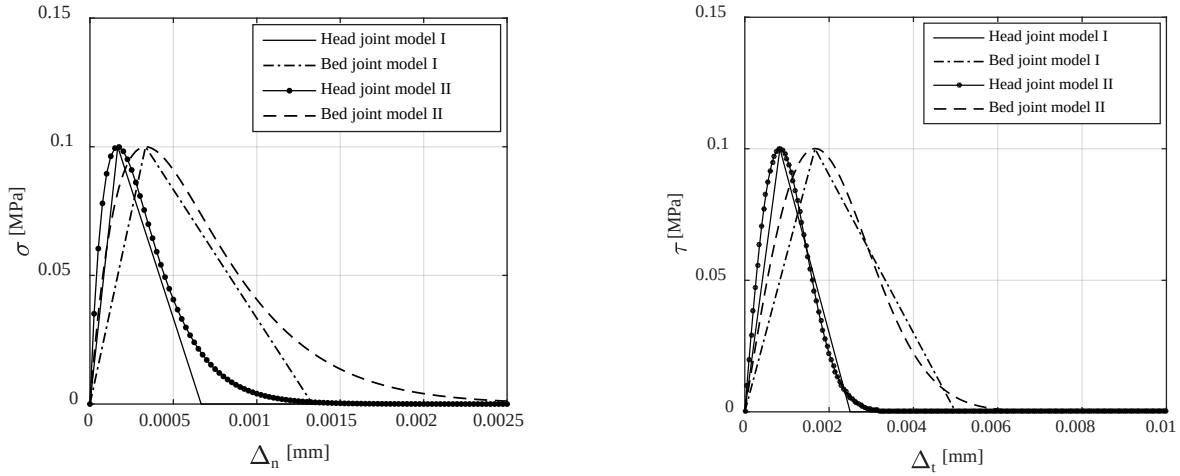

-a -b

Figure 6: Stress-jump of displacement curves adopted for the mortar joints interfaces (Header bond model): normal (-a) and tangential (-b) behavior.

4.2.1. Inelastic case, biaxial strain state

The two models presented in the previous sections are used here to perform a series of analyses at a cell level in the non-linear range under a biaxial strain state applied. The procedure allows estimating the homogenized stress and strain relationships at a fixed ratio between strains E_{xx} and E_{yy}, with a measuring strain given by $E_{nn} = \sqrt{E_{xx}^2 + E_{yy}^2}$. In Figure 7, the homogenized stress-strain curves obtained using the different models for masonry Type A are represented when an $E_{xx} \neq 0$ and $E_{yy} = 0$ strain state is applied up to failure of the RVE. In Figure 8, the stress-strain curves of the different triangular elements are depicted for these loading conditions, whereas in Figure 9 three deformed shapes of the RVE (elastic, peak and failure) are represented. The same results have been obtained the case $E_{xx} = 0$ and $E_{yy} \neq 0$, namely, in Figure 10, the homogenized stress-strain curves, in Figure 11, the stress-strain relationships on different elements, and, in Figure 12, the deformed shapes of the RVE.

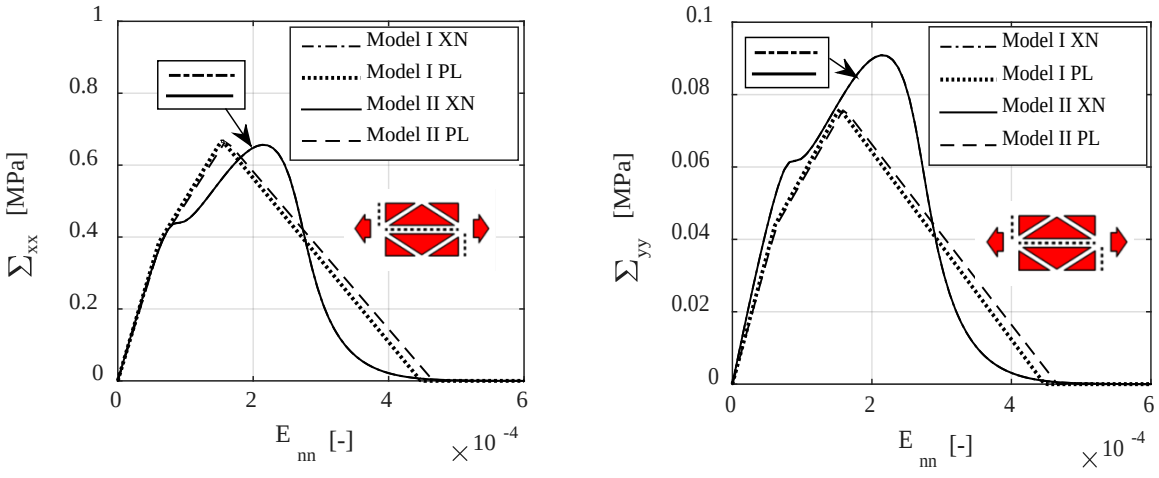

-a -b

Figure 7: Type A RVE, homogenized stress-strain behavior for $E_{xx} \neq 0$ $E_{yy} = 0$ (a) Σ_{xx} (b) Σ_{yy}.

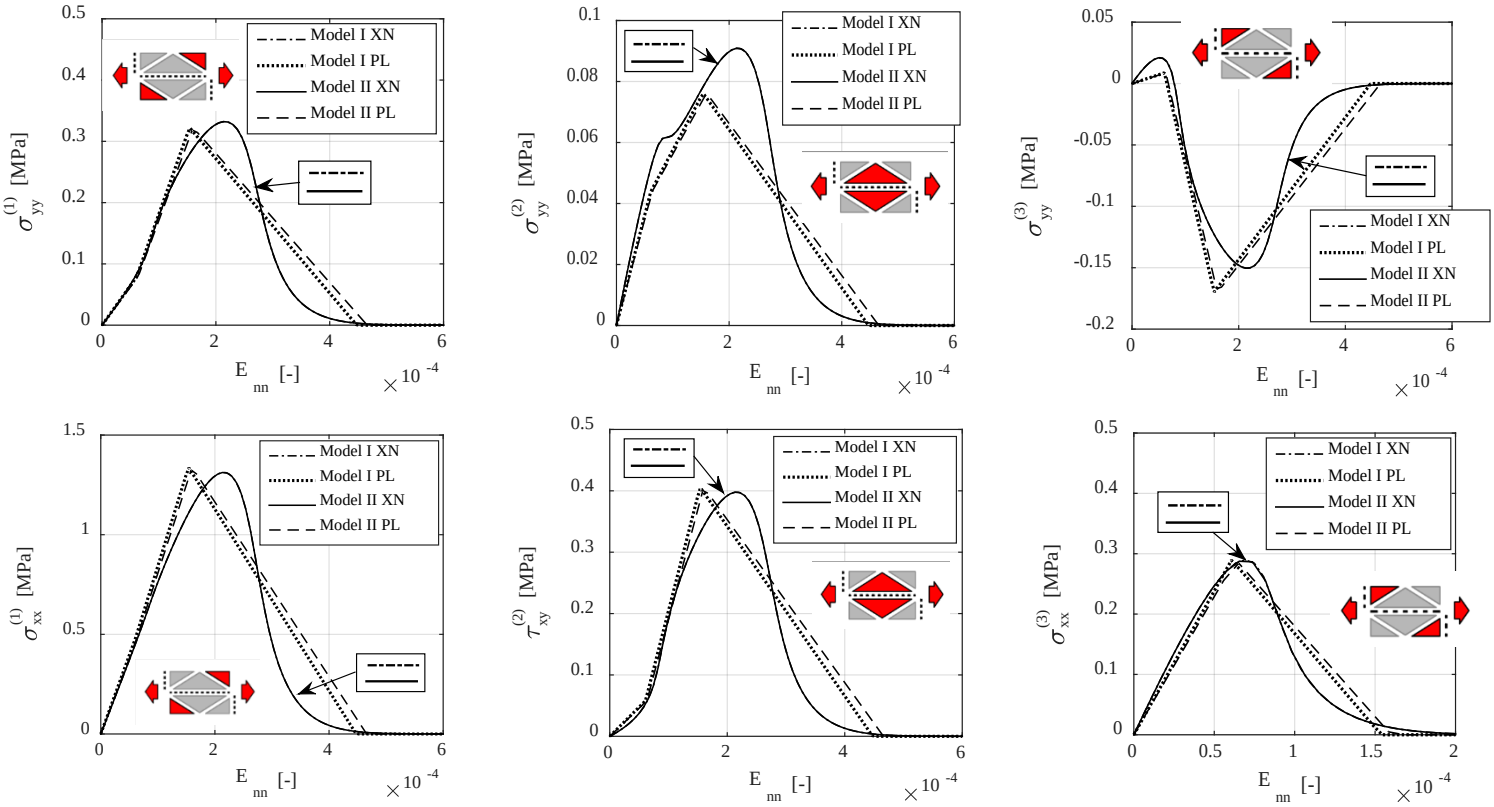

Figure 8: Type A RVE, stress strain curves on the different triangular elements for the application of $E_{xx} \neq 0$ and $E_{yy} = 0$.

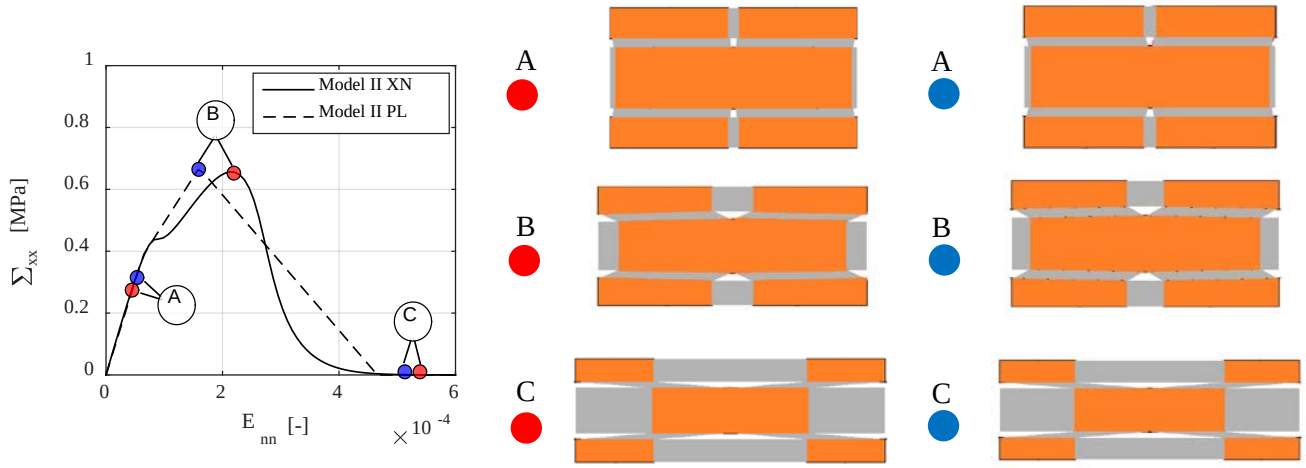

Xu-Needleman interface laws Piecewise linear interface laws

Figure 9: Type A RVE, deformed shape of the homogenized cell at different steps: A elastic phase, B peak load and C collapse and for different interface laws (XN and PL)

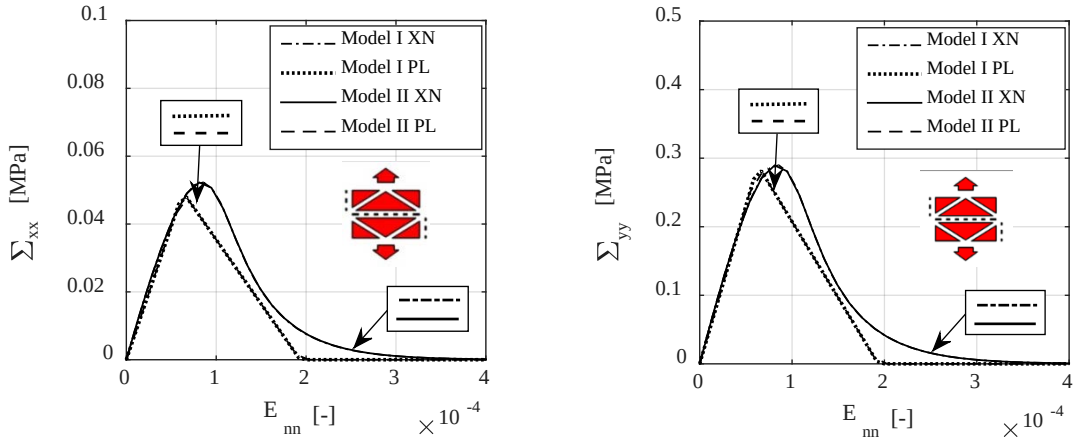

-a -b

Figure 10: Type A RVE, homogenized stress-strain behavior for $E_{xx} = 0$ $E_{yy} \neq 0$ (-a) Σ_{xx} (-b) Σ_{yy}.

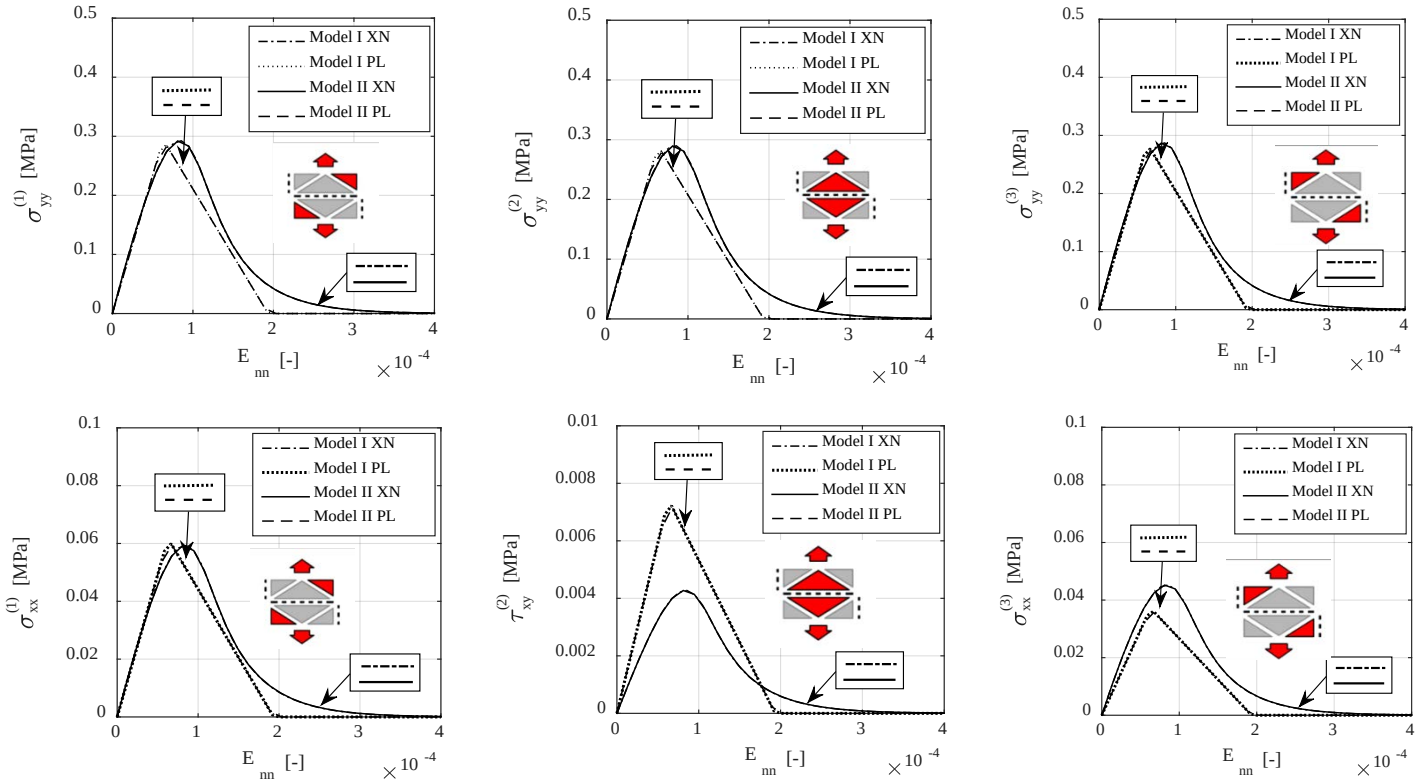

Figure 11: Type A RVE, stress strain curves on the different triangular elements for the application of $E_{xx} = 0 \quad E_{yy} \neq 0$.

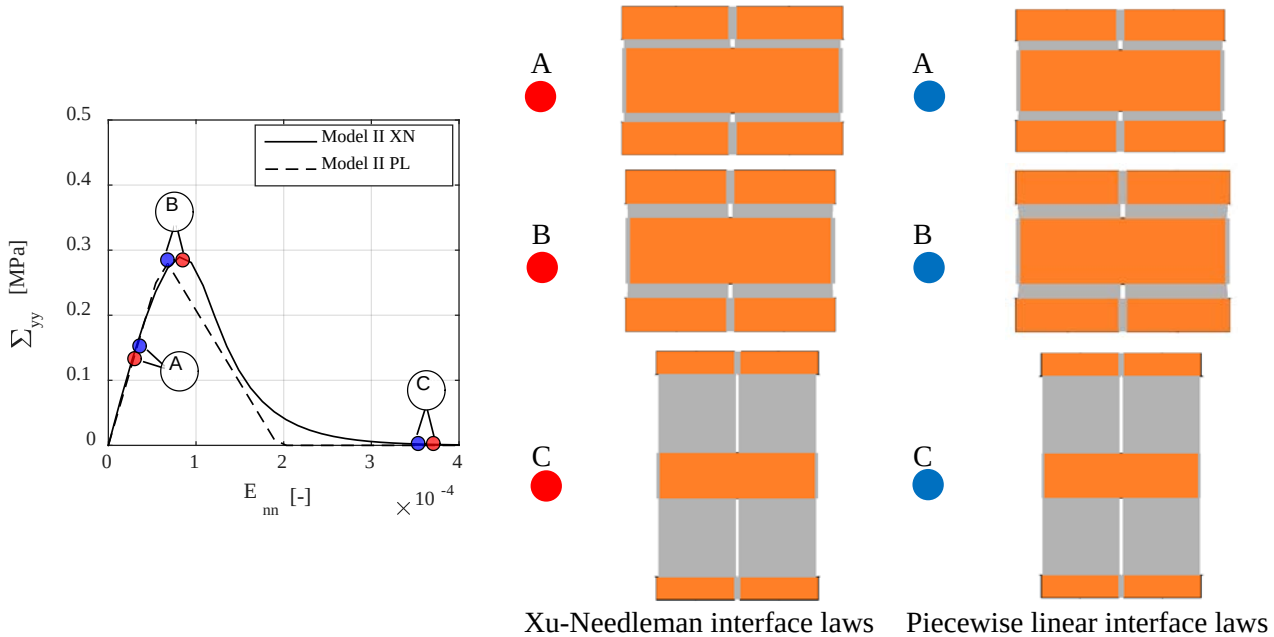

Figure 12: Type A RVE, deformed shape of the homogenized cell at different steps: A elastic phase, B peak load and C collapse and for different interface laws (XN and PL).

From a comparative analysis of the numerical results obtained, the following considerations may be done:

1. In case of $E_{xx} \neq 0$ and $E_{yy} = 0$ bed joints are subjected to considerable shear $\tau_{xy}^{(2)}$ (Figure 8), which contributes to a large strength and stiffness of the homogenized material under horizontal stretching (Figure 7), when compared to vertical stretching (Figure 10). Such an outcome is intuitively confirmed by the deformed shapes (compare for instance Figure 9 and Figure 12). In this latter case, the RVE failure mechanism is constituted by bed joint cracking under normal action, whereas in horizontal stretching the bed joint contributes in shear and head joints are subjected to tensile failure.
2. When uniaxial strain states (e.g. $E_{xx} \neq 0$ and $E_{yy} = 0$ or $E_{xx} = 0$ and $E_{yy} \neq 0$) are applied to the RVE a resultant biaxial stress state is obtained, as clearly visible in Figure 7 and Figure 10. This is not surprising, because of the staggered geometry of the joints and the Poisson's effect on elastic bricks. The phenomenon is much marked in horizontal stretching, because shear on element (2) is balanced (via equilibrium equations) by means of non-negligible vertical stresses on elements (1)-(3), as clearly visible in Figure 8.
3. Model I and Model II provide almost superimposable results, both when dealing with homogenized and local quantities, PL and XN interface models also furnish comparable output, with however some remarkable differences from an engineering standpoint, especially in the evaluation of transversal stresses. This is not surprising considering that XN model has a strong coupling between normal and shear components, whereas PL model is uncoupled.
4. One may finally argue if the very simplified mesh adopted for the RVE is able to provide reliable results when compared with more sophisticated (but also much demanding) meso-models, such as a classic refined discretization of the RVE into finite elements. Since a classic efficiency indicator of any homogenization method is commonly related to the deformation energy stored into the RVE, in Figure 13-a and –c respectively, deformation energies provided by the present simplified model and by a refined FE mesh in horizontal (subfigure –a) and vertical (subfigure –b) stretching are compared. When dealing with the refined FE model, 384 elastic triangles and 48 non-linear interfaces are utilized for bricks and mortar, respectively. As can be noted, results are almost superimposable and this is not surprising, since

in case of elastic bricks, vertical and horizontal strain components on the brick are respectively constant (subfigure –d) and fairly linear (subfigure –c) in case of vertical and horizontal stretching, respectively. Consequently, a single interface element can be used to properly represent head and bed joints, as done in the model proposed.

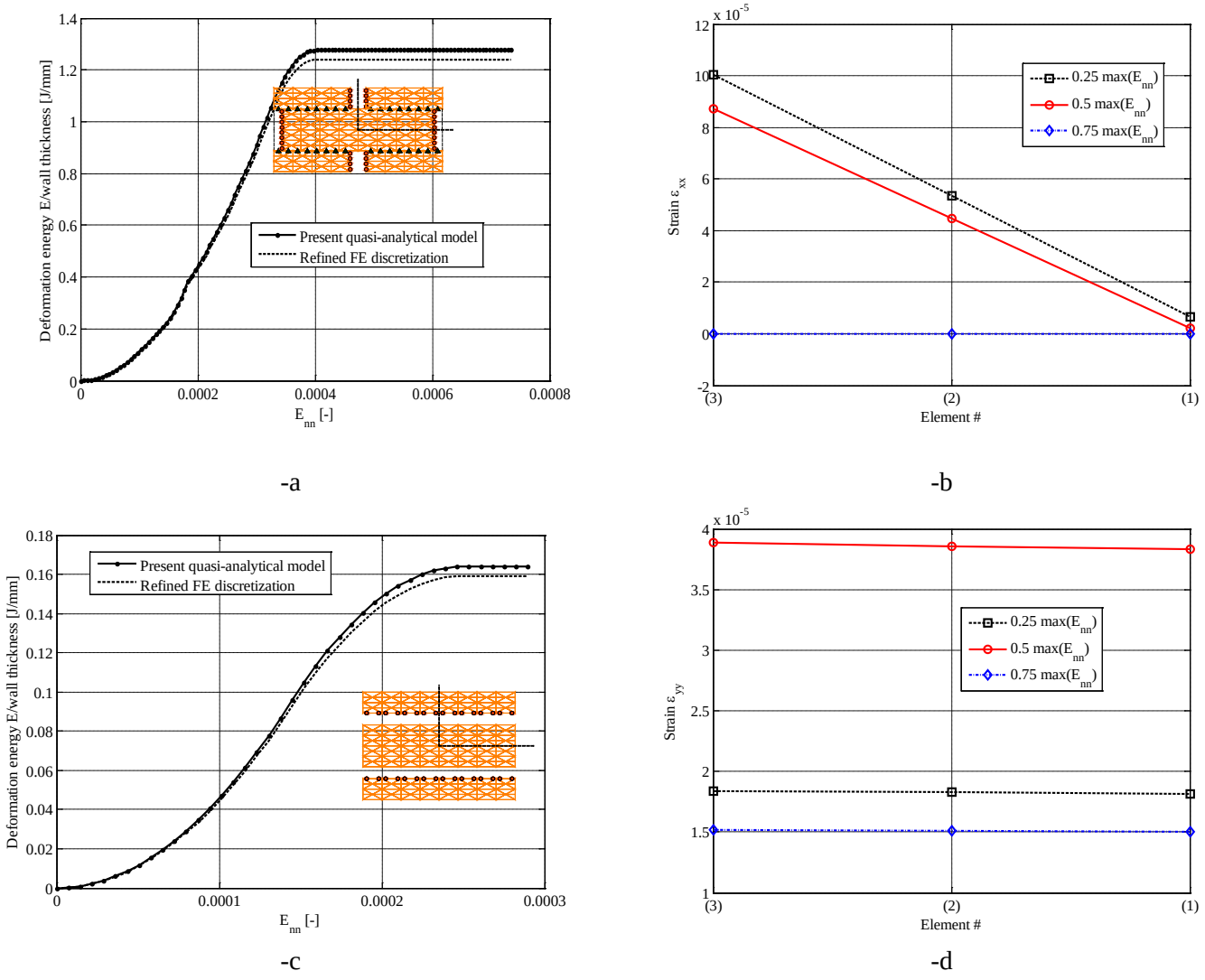

Figure 13: -a and –b: Type A RVE, stored deformation energy into the REV (-a: horizontal stretching, -b: vertical stretching) and (1)-(3) elements strains (-c: horizontal strain component in horizontal stretching, -d: vertical strain component in vertical stretching).

The same simulations were repeated for masonry Type B and the results provided by both models are summarized in Figure 14 and Figure 15 for horizontal and vertical stretching, respectively. The representation of the evolution

of local stresses on single elements is omitted for the sake of conciseness, showing a behavior identical to Type A masonry (see Figure 8 and Figure 11). The main difference between Type A and Type B masonry stands in the orthotropy ratio (both elastic and at peak), which obviously is much greater in stretcher bond pattern.

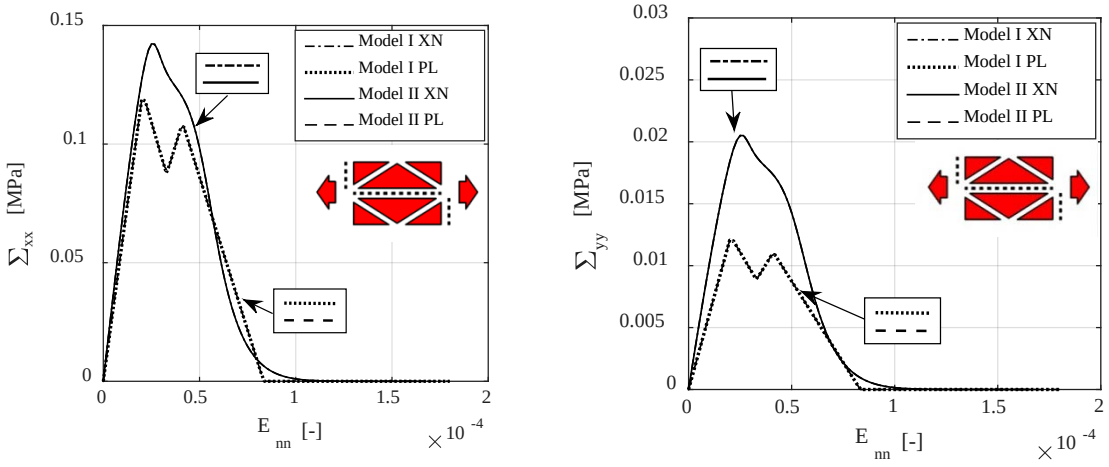

-a -b

Figure 14: Type B RVE, homogenized stress-strain behavior for $E_{xx} \neq 0$ $E_{yy} = 0$ (-a) Σ_{xx} (-b) Σ_{yy}.

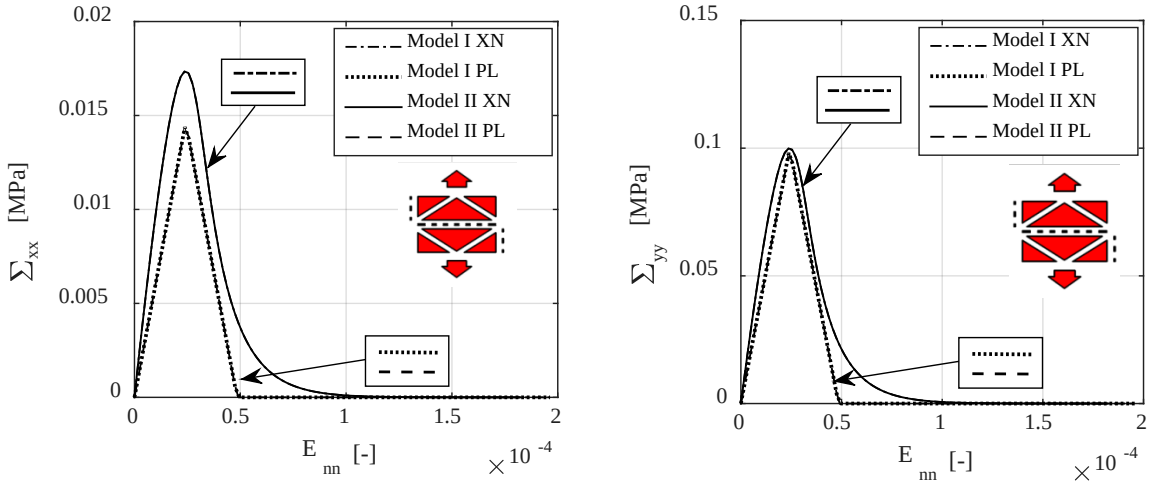

-a -b

Figure 15: Type A RVE, homogenized stress-strain behavior for $E_{xx} = 0$ $E_{yy} \neq 0$ (-a) Σ_{xx} (-b) Σ_{yy}.

4.2.2. Inelastic case, shear behavior results

In case of the application of a macroscopic shear deformation the homogenized response is as in Figure 16 (-a: Type A pattern; -b: Type B pattern). In Figure 17 and Figure 18 the deformed shapes of the elementary cell at different deformation levels (A elastic, B peak, C failure) are depicted. As it can be noted, high level of stress are reached mostly by the bed joints in both the non-linear laws implemented into the models.

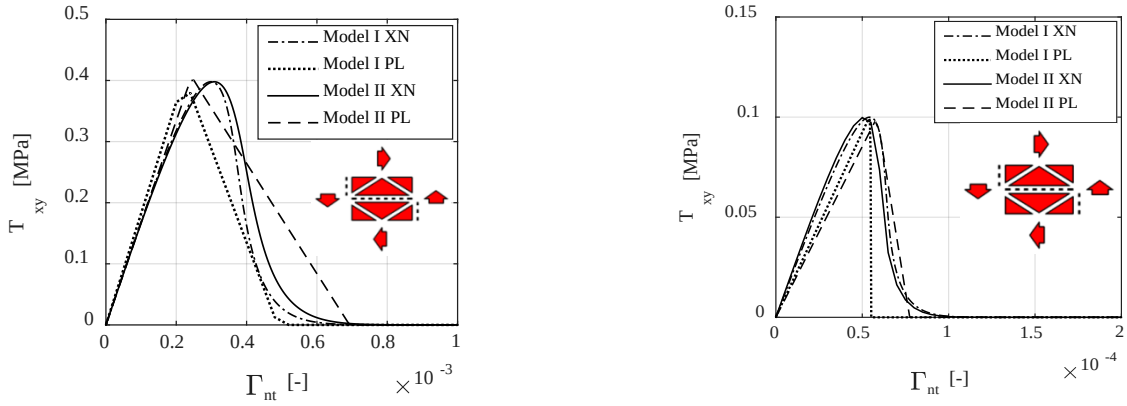

-a -b

Figure 16: Uniaxial homogenized shear response using the Model I for (-a) Type A RVE, stretcher bond masonry and (-b) Type B RVE, header bond masonry.

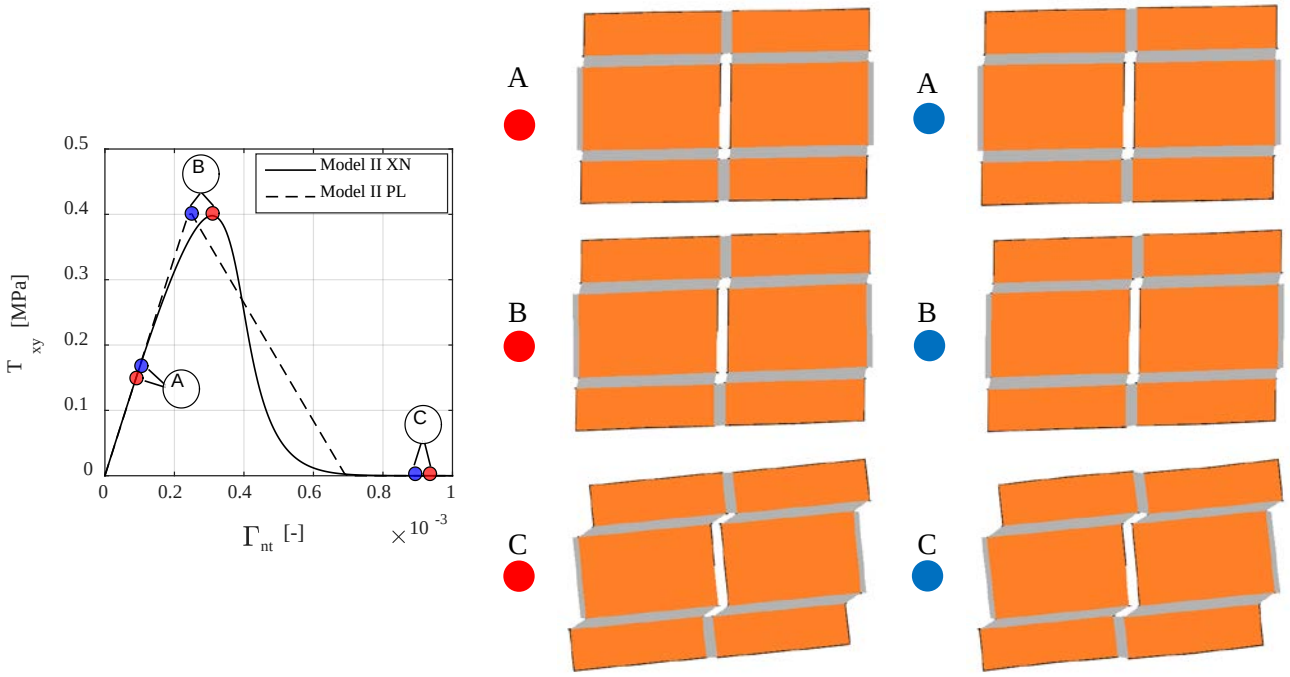

Figure 17: Deformed shape of the homogenized cell at different steps: A elastic phase, B peak load and C collapse (Stretcher bond) and for different interface laws (XN and PL).

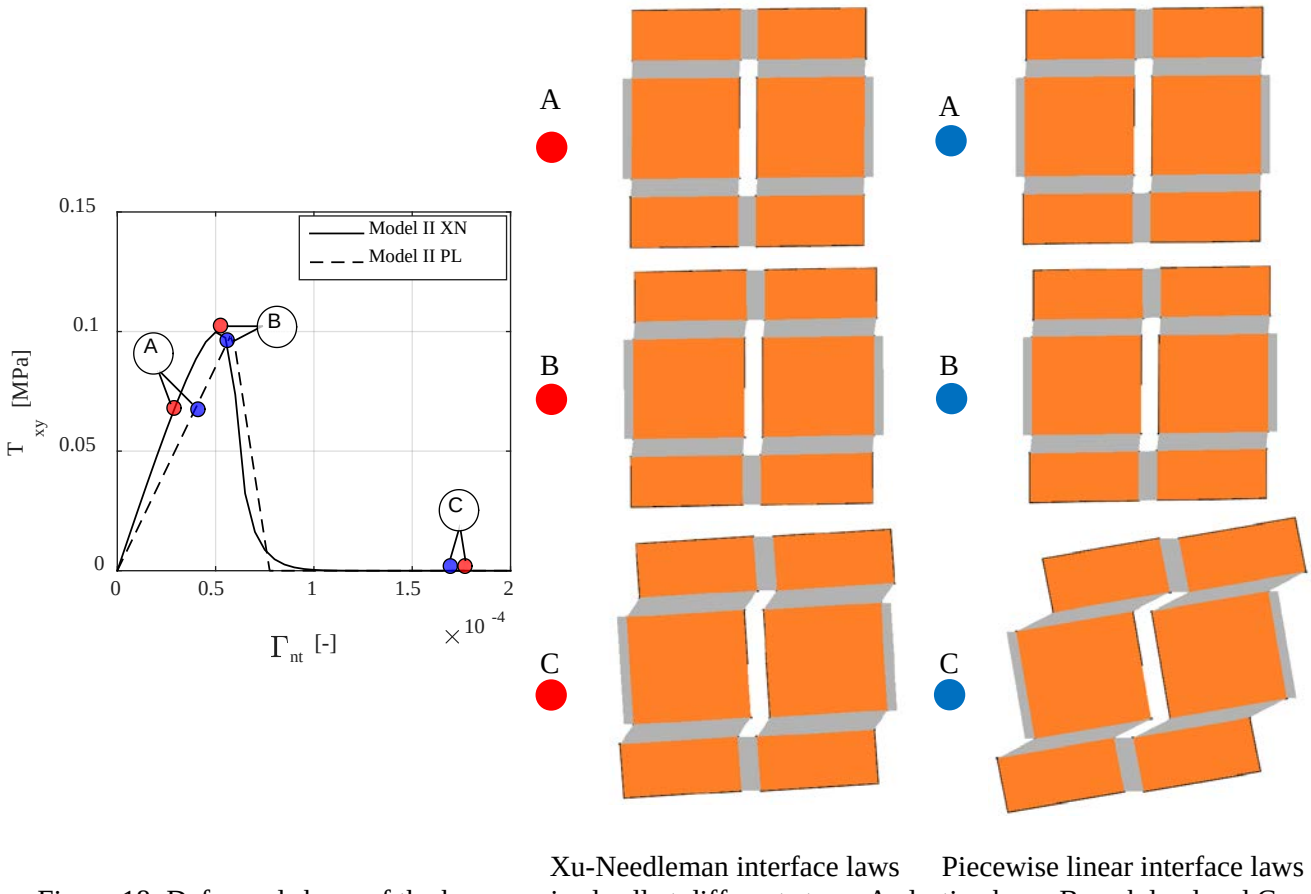

Figure 18: Deformed shape of the homogenized cell at different steps: A elastic phase, B peak load and C collapse (Header bond) and for different interface laws (XN and PL)

5. Structural implementation

In the present section, the homogenized mechanical properties deduced using the proposed models are implemented on an existing FE code to simulate structural elements. The aim is to show that the present models can be adopted by practitioners to the analysis of large scale structures, for which the classical micromechanical approach requires unpractical computational cost, and commercial codes. The simulations, carried out using Abaqus [28], deal with a series of masonry panels subjected to different load conditions for which experimental data are available in literature, as well as numerical results provided by other authors. The structural implementation is made with rigid infinitely resistant quadrilateral elements [38] and non-linear interfaces exhibiting an orthotropic behavior. On interfaces, the homogeneous masonry material is modeled with non-linear

shear/normal springs placed between adjoining rigid elements and characterized by the homogenized mechanical properties previously estimated. The homogenized stress-strain relationship to be used at structural level requires an identification of the spring elastic properties, in order to make the rigid-spring assemblage model compatible with the orthotropic continuum. Classically (see Kawai [38] for the general framework and recent applications for masonry by Casolo and co-workers [39]-[41]) such match is achieved in the linear elastic range by energy equivalence. Let us consider two rectangular rigid elements linked with a homogenized interface, having geometric properties as in Figure 19. Let us denote the dimensions of the rigid elements with "L" and "H", respectively for the length and the height, and the out of plane thickness with "t". The thickness of the interfaces is identified with "th". Under the application to the mechanical system of a normal displacement δ, the strain of the homogenized material is $\varepsilon = \frac{\delta}{2L+th}$, whereas the deformation of the springs is $\tilde{\varepsilon} = \frac{\delta}{th}$. The volumetric strain energies of the homogenized and rigid-spring models are:

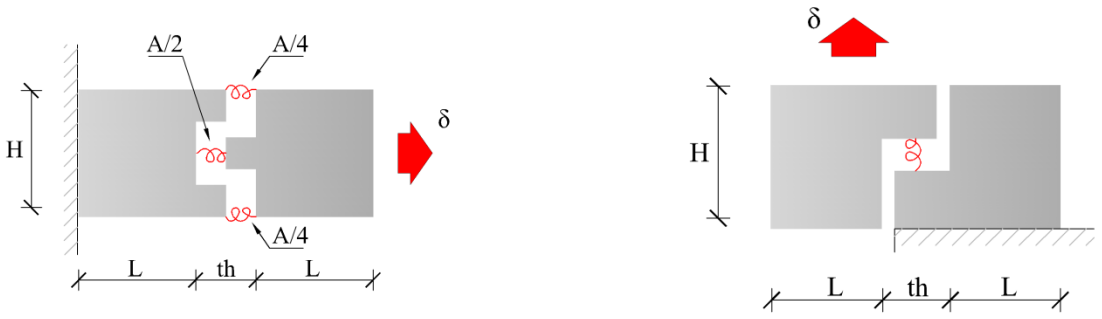

Figure 19: Springs identification: a- axial springs, b-shear spring.

$$U_{xx} = V \cdot \frac{1}{2} \cdot \sigma \cdot \varepsilon = \frac{1}{2} \cdot \frac{\delta^2}{2L+th} \cdot \tilde{E}_{xx} \cdot H \cdot t \qquad \text{a} \qquad (5)$$

$$U_{xx} = V \cdot \frac{1}{2} \cdot \sigma \cdot \varepsilon = \frac{1}{2} \cdot \frac{\delta^2}{th/2} \cdot E_{nxx} \cdot H \cdot t \qquad \text{b}$$

Where $\tilde{E}_{xx}$ is masonry homogenized elastic modulus along the horizontal direction, E_{nxx} is the elastic modulus of normal springs within the rigid elements and spring mass structural model and V is the volume of the mechanical system in Figure 19.

Equating the two energies, we obtain the elastic modulus of the axial (horizontal normal) springs as:

$$E_{nxx} = \frac{th/2 \cdot E_{xx}}{2L + th} \tag{6}$$

Using the same procedure it is possible to define E_{nyy} for vertical normal springs as:

$$E_{nyy} = \frac{th/2 \cdot E_{yy}}{H + th} \tag{7}$$

The determination of G_{nxy} follows an analogous procedure, see Figure 19-b, allowing an estimation of G_{xy} as follows.

$$U_{xy} = \frac{1}{2} \cdot \frac{\delta^2}{H/2} \cdot G_{nxy} \cdot th \cdot t \quad \text{a} \tag{8}$$

$$U_{xy} = \frac{1}{2} \cdot V \cdot \delta^2 \cdot G_{nxy} = \frac{1}{2} \cdot \frac{\delta^2}{2L + th} \cdot H \cdot t \quad \text{b}$$

$$G_{nxy} = G_{xy} \cdot \frac{H^2/4}{th \cdot (2L + th)} \quad \text{c}$$

6. Applications

6.1. Deep beam test

The first example here discussed deals with the well-known deep beam by Page [42]. The experimented wall has dimensions equal to 757x457 mm^2 and was tested up to collapse with a uniform pressure applied at the top edge with a steel beam, as shown in Figure 20-a . The masonry wall is built with half scale bricks with dimensions 122x37x54 mm^3 and 5 mm thick mortar joints. Figure 20-b reports the experimental collapse load by Page [42] and two numerical load-displacement curves found by Lourenço [43] and Milani [44], to compare with.

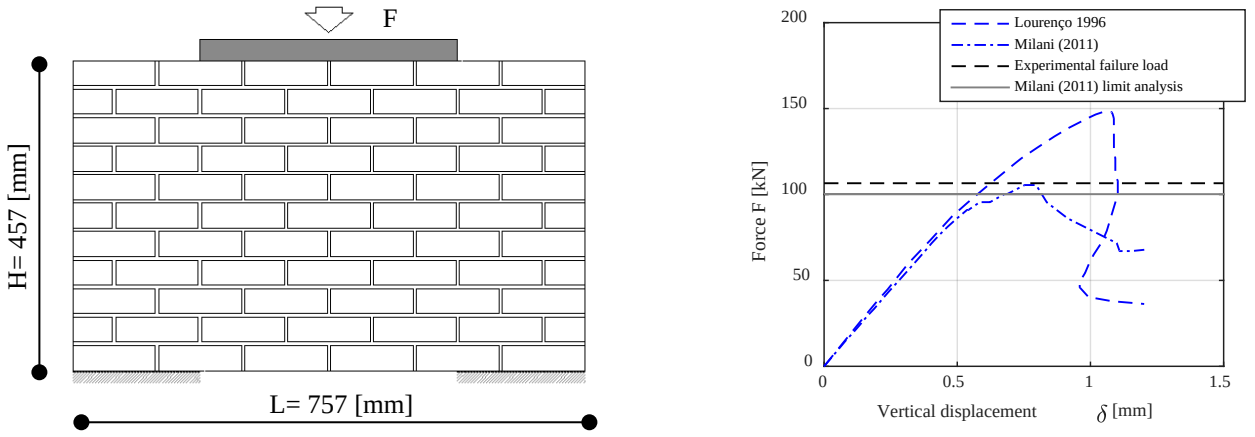

-a -b

Figure 20: Deep beam test by Page (geometry) and force-displacement curves/collapse loads obtained numerically/experimentally.

As can be noted only few information is available concerning the experimental tests developed, for which only the collapse load is reported. Mechanical properties adopted in the present simulations for the constituent materials are in agreement with the indications provided by Page [42] and recalled by Lourenço [43] in his work.

The mesh used to perform the analysis is shown in Figure 21-a, and is a fair compromise between numerical efficiency and accuracy of results. The identified elastic properties of the springs are the following: E_{nxx}= 360 MPa, E_{nyy}= 280 MPa, G_{nxy}=2840 MPa. Due to the symmetry of the masonry panels only one half of the geometry was reproduced. The results obtained numerically are shown in Figure 21-b. As can be observed, the model is able to reproduce quite accurately the collapse load of the masonry panel analyzed, that resulted extremely close to the experimental value reported by Page [42] (no other information is given by Page regarding pre- and post-peak behavior). A satisfactory agreement was also found between the results provided numerically by other researchers and those obtained using the present model, both in term of elastic and post peak phase. In fact, it is interesting to notice that the force displacement curve found with the present model is almost superimposable with that found by Milani in [44]. The models have the same internal discretization and a very similar non-linear constitutive behavior for the interfaces (which justifies the small differences found). The advantage of the present procedure is that, adopting a total displacement approach, the solution of the homogenization problem (meso-scale) is semi-analytical, whereas in [44] the procedure adopted is numerical (with coarse mesh). In combination with the adoption at a structural level of a discretization constituted by rigid elements and homogenized springs, a direct

implementation at the macro-scale of the homogenized stress-strain relationships found at the meso-scale is possible. Such a choice allows avoiding the utilization a classic nested multi-scale technique (which is computationally cumbersome), with a clear advantage on the computational costs.

In Figure 22, the deformed shapes of the structure obtained at three different instants (A: elastic limit, B: peak load, C: post peak, end of simulations) are depicted. In Figure 23, damage maps found numerically at the end of the simulations are represented. Shear failure is indicated by circles, horizontal axial failure is indicated by triangles and vertical axial failure is indicated by squares. Colors indicate the level of damage, so that incipient damage is indicated with blue color and full damage with red color. Subfigures –a and –b refer to compression and tension damage, respectively. It should be pointed out that, when a shear damage is present on the interface, depending if it associated with compressive or tensile behavior, it is represented either in subfigure –a or –b.

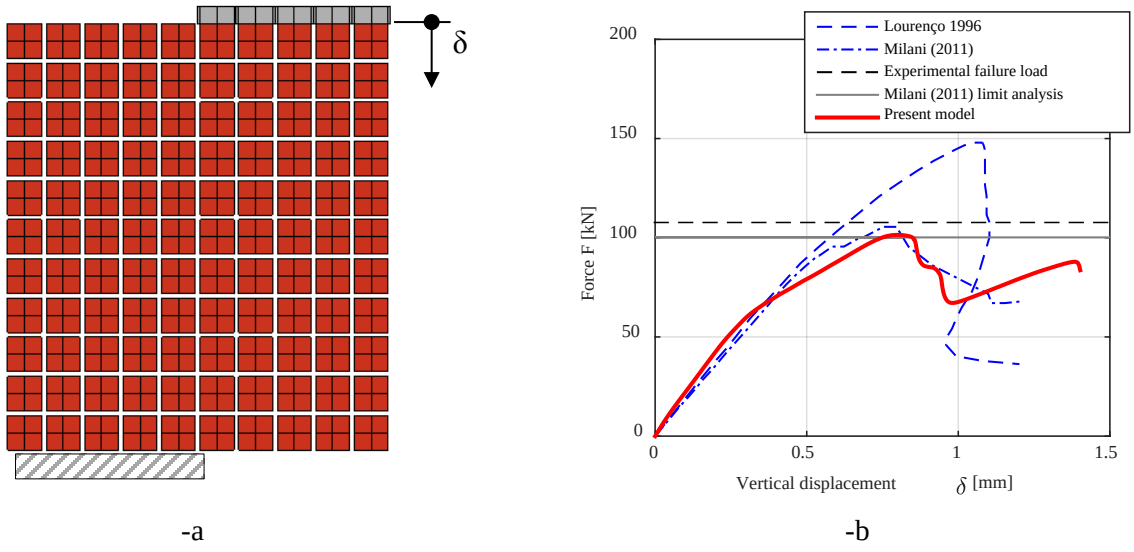

-a -b

Figure 21: Deep beam test, experimental set up by Page. –a: mesh adopted for the presented simulations. -b: results obtained with the presented model.

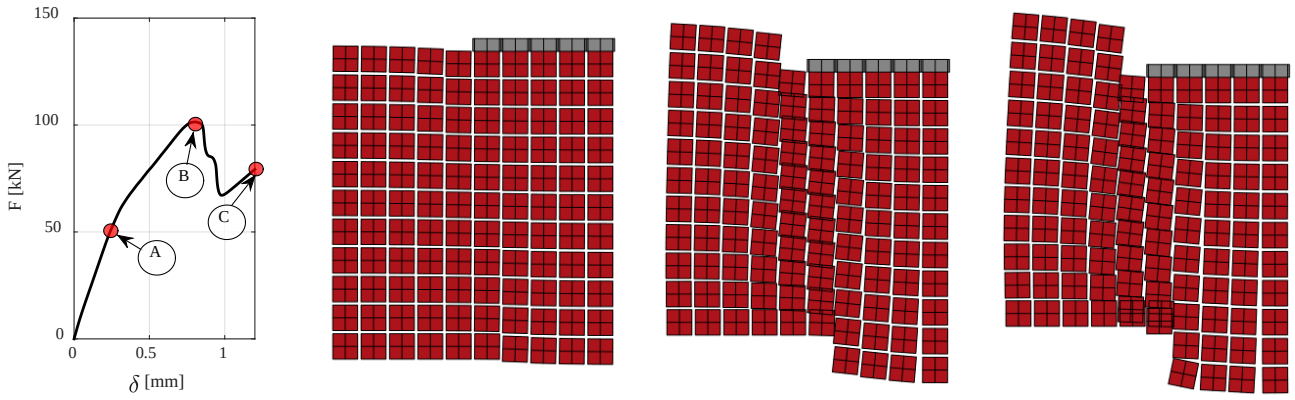

Figure 22: Deep beam test, deformed shapes at different instants (A: elastic limit; B: peak load; :C: end of simulations).

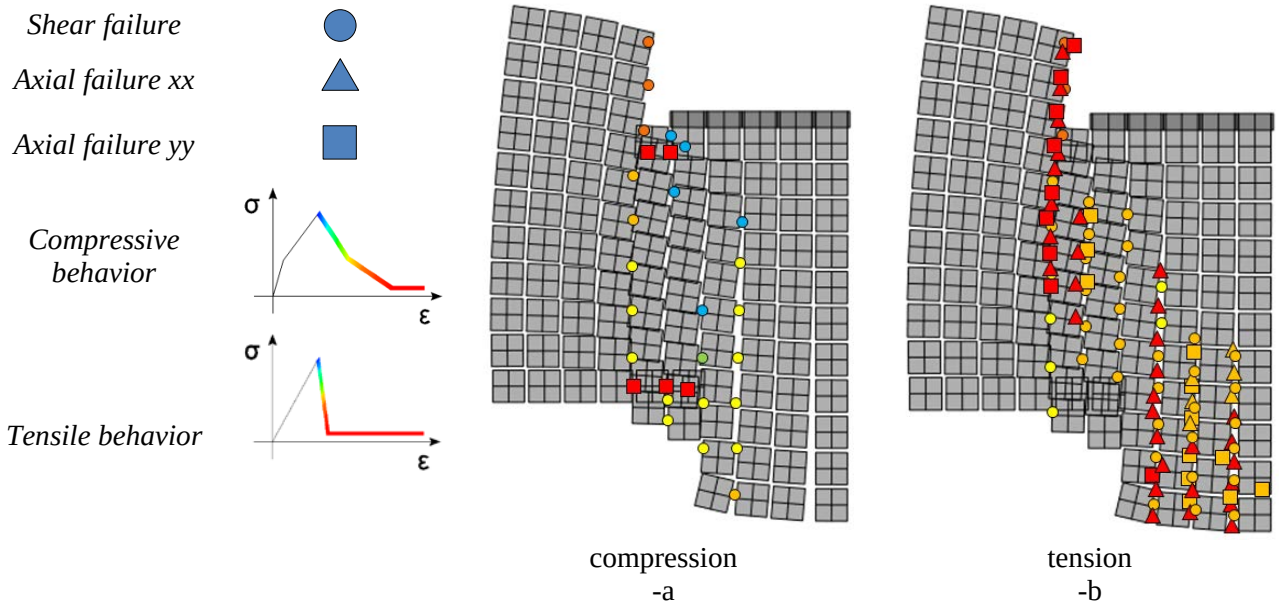

Figure 23: Deep beam test, damage pattern at the end of the simulations. –a: damage map in compression. –b: damage map in tension, at the end of the simulations.

As can be observed by a comparative analysis of deformed shape at collapse (Figure 22) and damage map distribution (Figure 23), the failure mode is characterized by the progressive formation of a compression strut from the steel beam to the support, with shear cracks on a vertical line at approximately ¼ of the length of the deep beam and with the appearance of compressive damages near the compressed toe. Conversely, tensile damage is

mainly concentrated along the vertical interfaces in the central zone of the panel, with the lower central part cracking under bending. It is finally interesting to notice that high level of damages spread along the vertical interfaces near the steel beam. This finding is probably due to the presence of stress concentrations under the extremes of the loaded edge.

6.1. Windowed shear panel

A windowed shear panel experimentally tested by Raijmakers and Vermeltfoort [45] is also here analyzed. The experimental test (two replicates) is carried out on panels of dimensions 990x1000 mm^2 with a central slight eccentric window one brick long and six bricks high, initially subjected to a pre-compression load of 0.3 MPa applied through a steel beam placed on the top edge, as shown in Figure 24-a. After having applied the vertical load, the structure is subjected to an increasing horizontal controlled displacement, up to the formation of a failure mechanism. Crack patterns and experimentally obtained load-displacement curves are depicted in Figure 24-b, where a series of other numerical curves are represented, namely those obtained by Milani [44] with an alternative homogenization approach and that provided by Lourenço and Rots in [46] using a heterogeneous model with joints reduced to Mohr-Coulomb interfaces with tension cutoff and elliptic cap in compression. During the load history, the rotation of the top beam is inhibited by the control of two actuators, a physical condition that is numerically taken into account imposing additional suitable constrains on mutual vertical displacement of the top edge corners. More information about the experimental campaign is available in [45] and the presence of the central window influences considerably the active failure mechanism, which is characterized by the formation of cracks zigzagging between bed and head joints roughly along one of the main diagonals, with a typical and clearly visible stepped pattern close to the opening corners, as shown in Figure 24-b.

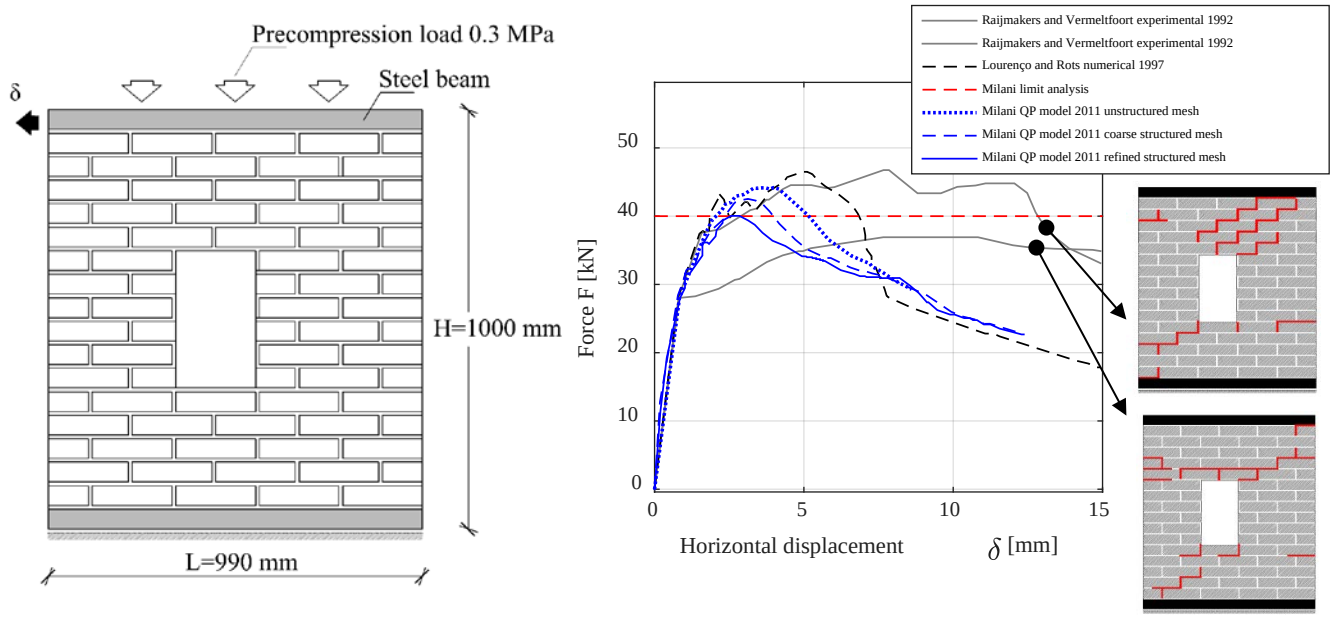

-a -b

Figure 24: Windowed shear panel, experimental setup with geometry (-a) and numerical results available in the literature (-b).

The masonry wall is constituted by bricks with dimensions equal to 210x52x100 mm^3, and mortar joints 10 mm thick. Mechanical properties adopted for bricks and mortar are identical to those assumed by Lourenço and Rots in their heterogeneous model, and are not reported here for the sake of conciseness. The reader is referred to [46] for a comprehensive mechanical characterization. The elastic identification of the interfaces conducted by means of the approach previously presented led to the utilization of the following elastic parameters at a structural level: elastic modulus for vertical interfaces E_{nxx} = 860 MPa, elastic modulus for horizontal interfaces E_{nyy} =372 MPa, and shear modulus G_{nxy} 2051 MPa.

The panel is discretized using 232 rigid quadrilateral elements with dimensions 52x52 mm^2, again a fair compromise between numerical efficiency and reliability of the expected results. A comparison among the results obtained experimentally, with numerical models from other authors and present load-displacement results is provided in Figure 25-b. As it can be noted, a quite good agreement is found in terms of elastic stiffness, peak load and post-peak behavior, especially with Milani model [44]. According with experimental evidence, the deformed shape at collapse shows that failure is due to the relative rotation of macro blocks inside the panel, as clearly visible

from Figure 26-point C, where the collapse mechanism is fully developed (compare for instance the formation of macro-blocks in point C with point B deformed shape). The damage map, as depicted in Figure 27, shows that inelastic deformation is mostly concentrated near the corners of the central opening and near the point of the application of the load, due to the high stresses arising in such areas.

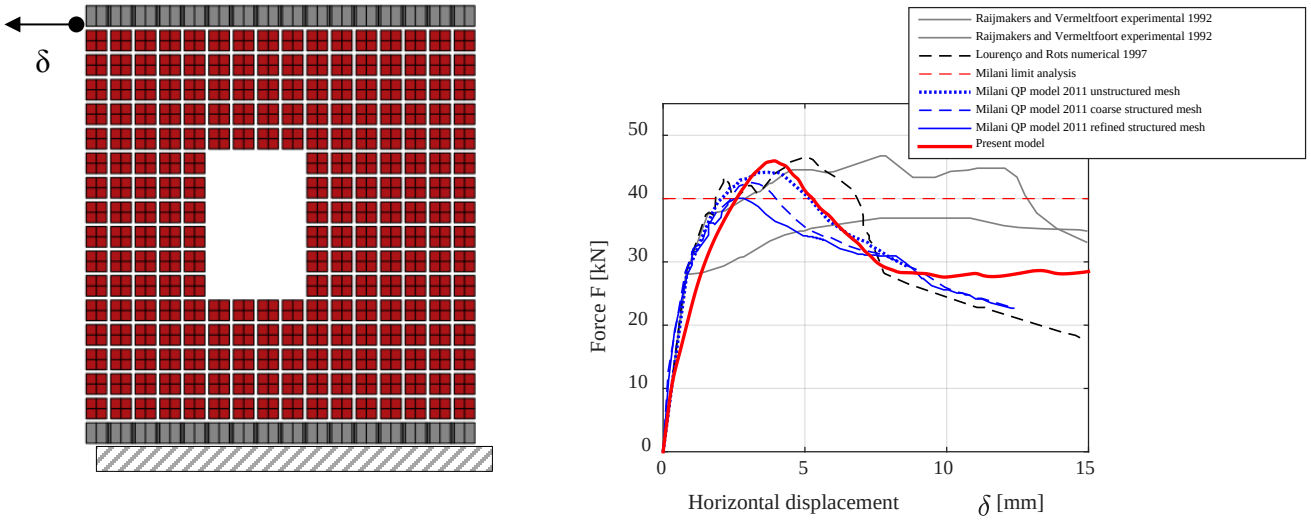

-a -b

Figure 25: Windowed shear panel. –a: mesh used for the numerical simulations, b- results obtained with the presented model

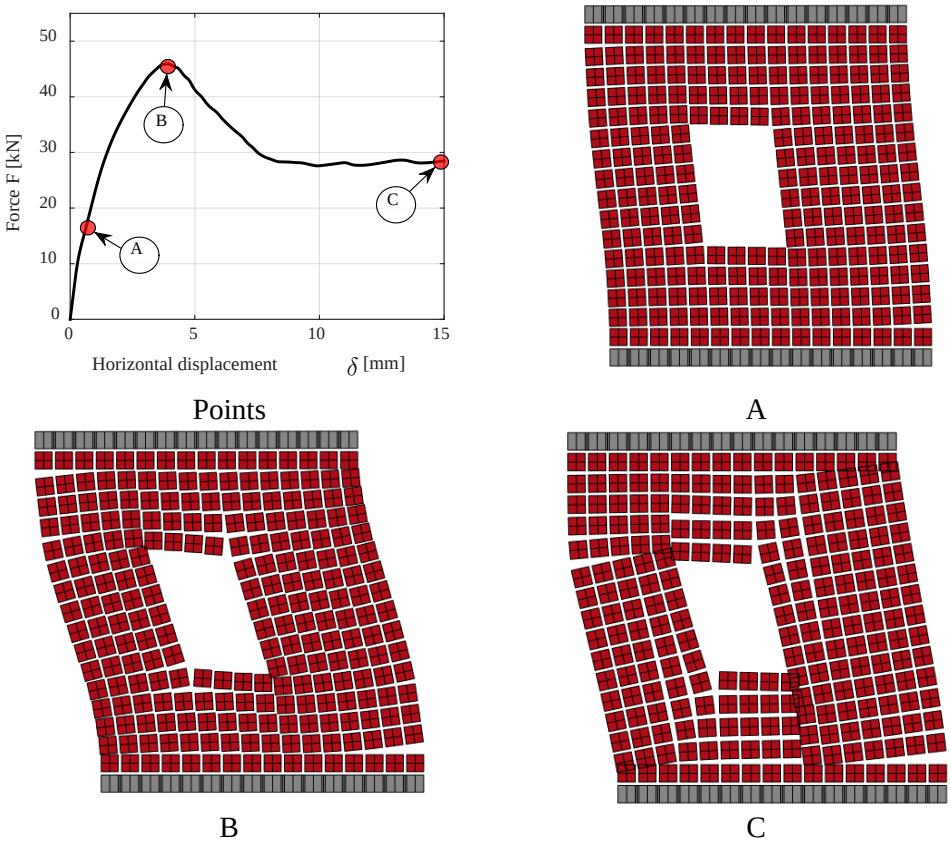

Figure 26: Windowed shear panel. Deep beam test, deformed shapes at different instants (A: elastic limit; B: peak load; :C: end of simulations).

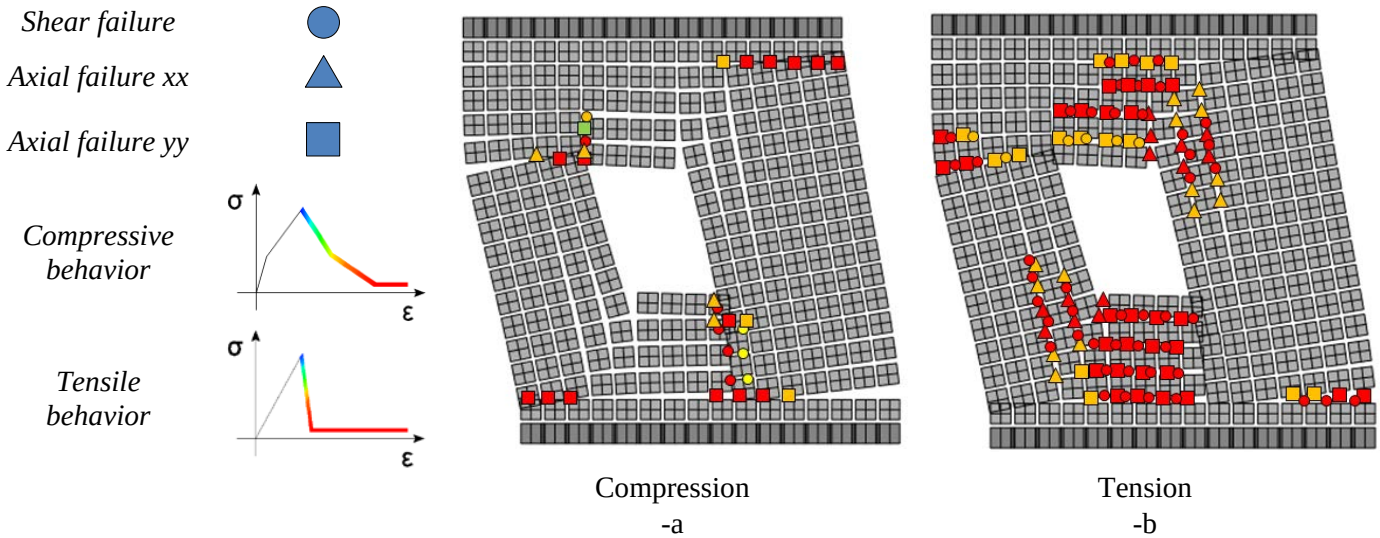

Figure 27: Windowed shear panel, damage pattern at the end of the simulations. –a: damage map in compression. – b: damage map in tension, at the end of the simulation.

6.2. ETH Zurich shear panels

The last set of simulations is devoted to the analysis of a masonry shear panel tested by Ganz and Thürlimann [47] at ETH Zurich some decades ago. The experimental campaign, which is now commonly used to benchmark new numerical models in the field of masonry modeling, was carried out with the aim of better understanding the structural behavior of three geometrically identical masonry panels under the combined action of different vertical pre-compressions and shear. Three different series of shear panels with almost the same geometry but under different loading conditions, labeled as W1, W2 and W3 where tested in [47]. Here, only shear panel W2 results are taken into consideration for the sake of conciseness. Authors experienced a similar performance of the model when applied to panels W1 and W3 and the reader is referred to [48] for a detailed discussion of the numerical results obtained. The walls have in-plane dimensions equal to 3600x2000 mm^2 (width x height), see Figure 28-a. Hollow clay bricks of dimensions equal to 300x200x150 mm^3 were used, whereas the thickness of the joints is assumed equal to 10 mm. Two stiff masonry flanges are present in correspondence of vertical edges and a thick heavy concrete plate was put on the top, to properly apply and distribute the desired vertical pre-compression load, variable depending on the sample tested, Figure 28-a. WP1 and WP2 are subjected, prior the application of the horizontal load, to a distributed vertical pre-compression equal respectively to 0.61 and 1.91 MPa, whereas a concentrated eccentric load equal to 422 kN is applied on the top edge of panel WP3, as illustrated in Figure 28-a. The width of the flanges is equal to a single brick and their out-of-plane thickness is equal to 600 mm for WP1 and WP2 and 840 mm for WP3. The utilization of hollow bricks makes convenient the utilization at a structural level of the homogenized stress strain relationships depicted in Figure 29, appearing reasonably in agreement with those used in the technical literature to numerically reproduce the present experimental studies. Concerning the mechanical properties adopted for the present simulations, a low tensile strength is assumed in vertical direction, whilst along the horizontal direction a peak strength value equal to 0.28 MPa is used, in order to suitably take into account the brick perforation. The identified elastic parameters implemented into the FE commercial code are the following: elastic modulus for vertical interfaces E_{nxx} =112 MPa, elastic modulus for horizontal interfaces E_{nyy} =150 MPa, shear modulus G_{nxy} =10000 MPa. Regarding the properties of the flanges, some indications are

reported by Lourenço [43] in terms of maximum tensile and compressive strength. For the present simulations, a value equal to 0.28 MPa is assumed in tension, while 2.2 MPa is adopted in compression.

Experimental evidences shown that during the first phase of application of the horizontal imposed displacement, diagonal cracks started to occur with a typical stepped pattern, while at the end of the tests the collapse mechanism is characterized by the formation of flexural hinges on both flanges. All panels, but especially WP2 which has a high pre-compression level, exhibited a global experimental ductile behavior, see Figure 28–b, where experimental curves and numerical results (both obtained with the present model and commented in the sequel, a by Lourenço [43]) are represented. Such rather unusual response for shear walls can be reasonably explained with the confinement action produced by the flanges and the concrete slab. Present simulations are carried out initially imposing the pre-compression load and then applying to the structure the horizontal displacement. The relative rotation of the top edge of the panel is allowed during the entire load history, in agreement with real experimental conditions. This fact produces numerically high levels of compression stress located in the right flange that, in agreement with the experimental evidence, exhibits for WP2 a partial failure with the formation of rotational plastic hinges. The panel is discretized by means of a fairly refined mesh constituted by 210 rigid elements (dimensions equal to 150x190 mm^2), Figure 30.

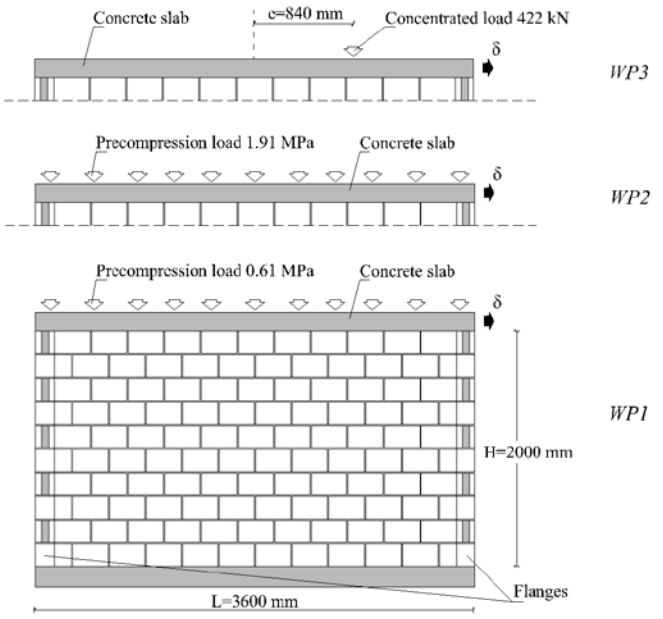

-a

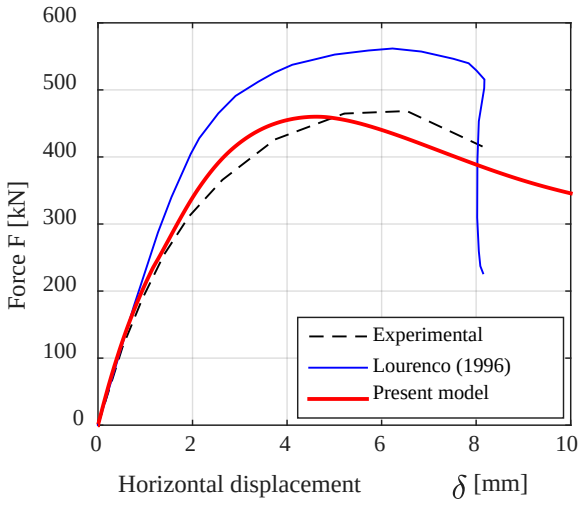

WP2

-b

Figure 28: ETHZ shear walls, experimental setup (-a) and force displacement results (-b) for WP2 test

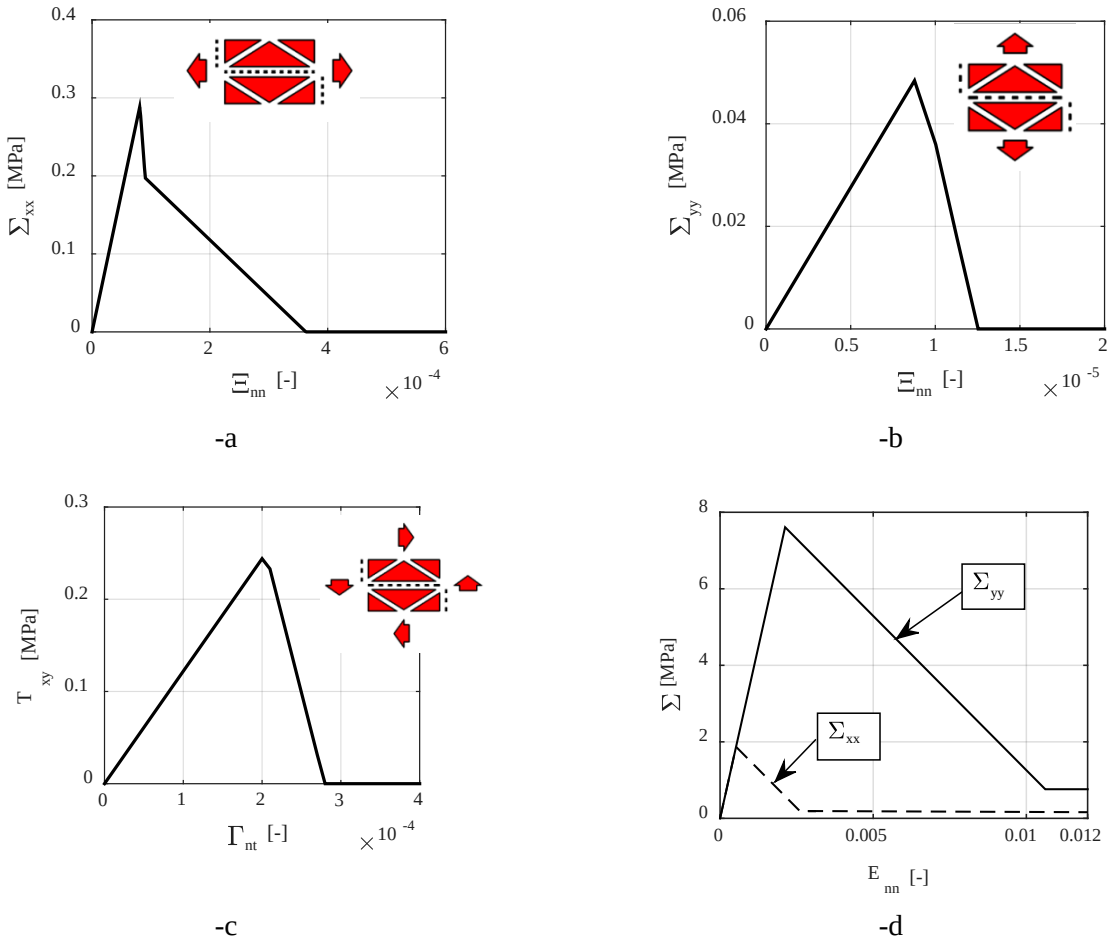

Figure 29: ETHZ shear walls, homogenized stress strain relationships adopted at a structural level. –a: horizontal tensile stress behavior. –b: vertical tensile stress behavior. –c: shear stress behavior. –d: compression behavior.

As already pointed out, in Figure 28-b global force-displacement curves obtained numerically are compared with experimental ones and those provided by Lourenço [43] with a macroscopic orthotropic elasto-plastic model. As can be noted, rather satisfactory agreement is found. Even the extremely ductile behavior of the specimens seems well reproduced by the proposed approach.

Deformed shapes at three different instants (A: elastic; B: peak; C: end of simulations) and resultant crack patterns are summarized in Figure 30. The deformed shape of the panel at the end of the simulations exhibits some common features with experimented ones, as for instance the formation of a well-defined plastic hinge near the base of the right flange and localization of crushing, i.e. compression failure, in the lower right part of the shear wall, plus the

formation of a diagonal strut. As a matter of fact, even if the typical stepped cracks experienced during the loading history cannot be reproduced by any homogenization approach, the deformed shape obtained at the end of the simulations clearly shows the formation of a shear band running on the diagonal compressed strut.

A visible rotation of the concrete slab is also worth noting, with the formation of a clear region undergoing tensile failure, spreading considerably thanks to the combined effect of pre-compression and concrete slab rotation. The compressed toe on the right, indeed, exhibits high stress values, compensated by the tensile stress region spreading.

A mixed shear-crushing failure is also clearly visible near the lower right flange, showing several similarities with experimental evidences.

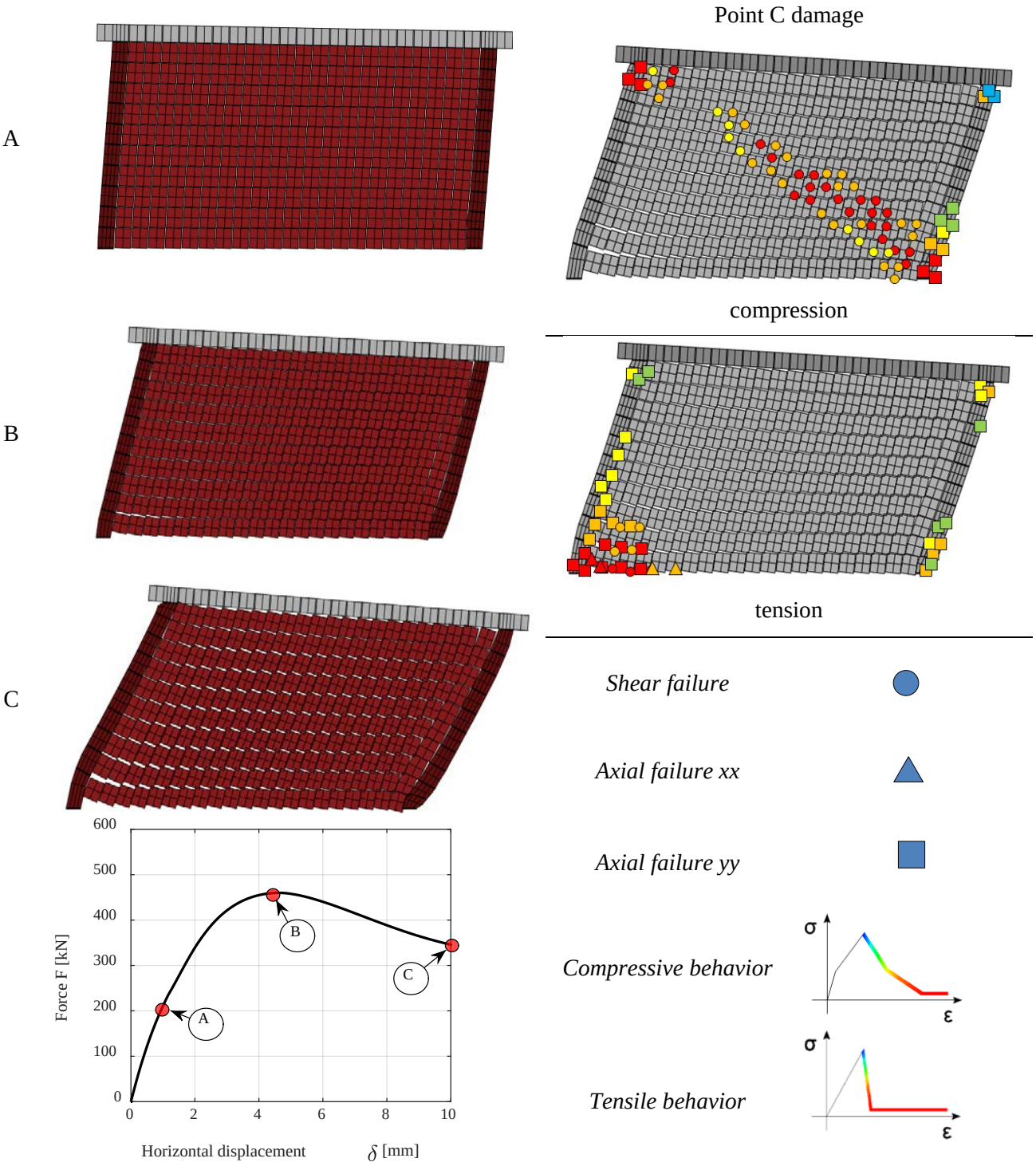

Figure 30: ETHZ shear panel WP2, deformed shapes at progressive imposed horizontal deformation and corresponding damage patterns at the end of the simulations.

7. Conclusions

Two very simple identification approaches for the non-linear analysis of masonry structures in-plane loaded have been presented and implemented in a commercial FE software for the analysis of full scale structures. At a cell level, the mechanical system is constituted by a rectangular elementary cell where bricks are discretized by means of a few triangular elastic FEs and joints are reduced to interfaces with a holonomic non-linear behavior. The first approach is a mechanical model translating mathematically into a system of few non-linear equations, whereas the second is a quasi-analytical procedure that keeps as unknowns only two kinematic variables. Homogenized stress-strain diagrams so obtained, after a comprehensive benchmark, are utilized at a structural level for the analysis of entire structures, by means of a discretization with rigid quadrilateral elements interconnected by holonomic homogenized and non-linear shear-normal springs. Several example of technical relevance have been discussed, showing always the excellent stability and reliability of the model proposed. The main innovative aspects are twofold: (a) At a cell level, the FE discretization adopted allows for a determination of the homogenized stress-strain behavior by means of a minimal computational effort; (b) At a structural level, the procedure is directly implemented into any general purpose FE commercial code.

Finally, it is worth mentioning that the model proposed compares favorably (as far as the numerical efficiency is concerned, see Tab. 2) with a standard heterogeneous approach, where brick and joints are modeled separately, directly at a structural level. In particular, in this latter approach each brick is meshed with four noded rectangular finite elements (four columns and two rows of elements) and joints are reduced to interfaces with the same constitutive behavior used in the homogenization model (multi-linear softening model with friction). Computations have been performed on a single WS equipped with 4 parallel CPUs with 8 Gb RAM and without parallelization. Systematically, authors experienced a numerical efficiency of the homogenized approach much higher, suggesting that the procedure proposed is particularly suited for analyses of entire structures and large scale walls, all situations where any heterogeneous approach would be presumably subjected to numerical issues and premature halting, despite parallelization with large Work Stations can help in the reduction of the still too long processing times needed.

Test	CPU time for obtaining homogenized stress strain curves (meso scale)	CPU time to solve the structural problem (macro-scale)	CPU time to solve the meso- and macro-scale problems	CPU time to solve the structural problem with a heterogeneous approach
	MeSc-t	MaSc-t	Homo-t=MeSc-t+MaSc-t	Hete-t
Unit of Measure	hh:mm:ss	hh:mm:ss	hh:mm:ss	hh:mm:ss
Deep beam test	00:01:44	00:12:20	00:14:04	04:27:09
Windowed shear panel	00:02:02	00:09:19	00:11:21	07:12:01
ETHZ shear wall	00:00:33	00:15:01	00:15:34	09:03:57

Tab. 2. Computational efficiency of the numerical model proposed. CPU times needed to solve the homogenization problem (Homo-t) compared with CPU times required by a heterogeneous approach (bricks meshed with 8 quadrilateral elements and joints reduced to interfaces with frictional behavior identical to those used in the homogenization model).

8. References

[1] Di Pasquale S. New trends in the analysis of masonry structures. Meccanica 1992; 27: 173-184.

[2] Berto L, Saetta A, Scotta R, Vitaliani R. An orthotropic damage model for masonry structures. Int J Numer Methods Engng 2002; 55: 127–57.

[3] Lourenço PB, de Borst R, Rots JG. A plane stress softening plasticity model for orthotropic materials. International Journal for Numerical Methods in Engineering 1997; 40: 4033-4057.

[4] Milani G. Four approaches to determine masonry strength domain. Proceedings of ICE, Engineering and Computational Mechanics 2015; 168(3): 99-121.

[5] Lourenço PB, Rots J. A multi-surface interface model for the analysis of masonry structures. Journal of Engineering Mechanics ASCE 1997; 123 (7): 660-668.

[6] Lotfi HR, Shing PB. Interface model applied to fracture of masonry structures. Journal of Structural Engineering ASCE 1994; 120 (1): 63-80.

[7] Sutcliffe DJ, Yu HS, Page AW. Lower bound limit analysis of unreinforced masonry shear walls. Computers & Structures 2001; 79: 1295-1312.

[8] Pietruszczak S, Ushaksarei R. Description of inelastic behavior of structural masonry. International Journal of Solids and Structures 2003; 40: 4003–19.

[9] Gambarotta L, Lagomarsino S. Damage models for the seismic response of brick masonry shear walls. Part I: the mortar joint model and its applications. Earthquake Engineering and Structural Dynamics 1997; 26: 423–439.

[10] de Buhan P, de Felice G. A homogenisation approach to the ultimate strength of brick masonry. Journal of the Mechanics and Physics of Solids 1997; 45 (7): 1085-1104.

[11] Luciano R, Sacco E. Homogenisation technique and damage model for old masonry material. International Journal of Solids and Structures 1997; 34 (24): 3191-3208.

[12] Adessi D., Sacco E. A kinematic enriched plane state formulation for the analysis of masonry panels. European Journal of Mechanics – A/Solids 2014; 44: 188-200.

[13] Pegon P, Anthoine A. Numerical strategies for solving continuum damage problems with softening: application to the homogenisation of masonry. Computers & Structures 1997; 64 (1-4): 623-642.

[14] Anthoine, A. Derivation of the in-plane elastic characteristics of masonry through homogenization theory. International Journal of Solids and Structures 1995; 32(2): 137–163.

[15] Milani G. Homogenized limit analysis of FRP-reinforced masonry walls out-of-plane loaded. Computational Mechanics 2009; 43: 617–639.
[16] Milani G, Lourenço PB, Tralli A. Homogenised limit analysis of masonry walls. Part I: failure surfaces. Computers & Structures 2006; 84(3-4): 166-180.
[17] Milani G, Lourenço PB, Tralli A. Homogenization approach for the limit analysis of out-of-plane loaded masonry walls. Journal of Structural Engineering ASCE 2006; 132(10): 1650-1663.
[18] Milani G, Lourenço PB. Monte Carlo homogenized limit analysis model for randomly assembled blocks in-plane loaded. Computational Mechanics 2010; 46(6): 827-849.
[19] Massart T, Peerlings RHJ, Geers MGD. Mesoscopic modeling of failure and damage-induced anisotropy in brick masonry. Eur J Mech A/Solids 2004; 23:719–35.
[20] Colliat JB, Davenne L, Ibrahimbegovic A, Modélisation jusqu'à rupture de murs en maçonnerie chargés dans leur plan. Revue francaise de génie civil 2002; 4: 593-606.
[21] Xu XP, Needleman A. Potential-based and non-potential-based cohesive zone formulations under mixed-mode separation and over-closure. Part I: Theoretical Analysis 1993; 2:417-418
[22] McGarry P, Máirtín EO, Parry G, Beltz GE. Potential-based and non-potential-based cohesive zone formulations under mixed-mode separation and over-closure. Part I: Theoretical analysis. Journal of the Mechanics and Physics of Solids 2014; 63: 336–362.
[23] Fedele R. Simultaneous Assessment of mechanical properties and boundary conditions based on Digital Image Correlation. Experimental Mechanics 2015; 55(1): 139-153.
[24] Kamiński M. Sensitivity and randomness in homogenization of periodic fiber-reinforced composites via the response function method. Int. J. Solids & Struct. 2009; 46(3): 923-937.
[25] Suquet P. Analyse limite et et homogeneisation. Comptes Rendus de l'Academie des Sciences - Series IIB – Mechanics 1983; 296: 1355-1358.
[26] Cecchi A, Milani G, Tralli A. A Reissner-Mindlin limit analysis model for out-of-plane loaded running bond masonry walls. International Journal of Solids and Structures 2007; 44(5): 1438-1460.
[27] Matlab User's Guide 2007. http://www.mathworks.com/products/matlab/
[28] ABAQUS™. Theory manual, version 6.6; 2006.
[29] Milani G, Bertolesi E. Holonomic homogenized approach for the non-linear analysis of in-plane loaded masonry panels. Under review.
[30] van den Bosch MJ, Schreurs PJG, Geers MGD. An improved description of the exponential Xu and Needleman cohesive zone law for mixed-mode decohesion. Engineering Fracture Mechanics 2006; 73: 1220–1234.
[31] Liu PF, Gu ZP,·Peng XQ. A nonlinear cohesive/friction coupled model for shear induced delamination of adhesive composite joint. International Journal of Fracture 2016; 199:135–156.
[32] Taliercio A. Closed-form expressions for the macroscopic in-plane elastic and creep coefficients of brick masonry. International Journal of Solids and Structures 2014; 51(17): 2949-2963.
[33] Pande G.N, Liang J.X, Middleton J. Equivalent elastic moduli for brick masonry. Computers and Geotechnics 1989; 8: 243–265.
[34] Drougkas A, Roca P, Molins C. Analytical micro-modeling of masonry periodic unit cells – Elastic properties. International Journal of Solids and Structures 2015; 69-70: 169-188.
[35] Cecchi A, Milani G, Tralli A. Validation of analytical multiparameter homogenization models for out-of-plane loaded masonry walls by means of the finite element method. Journal of Engineering Mechanics ASCE 2005; 131(2): 185-198.
[36] Lourenço P.B. On the use of homogenisation techniques for the analysis of masonry structures. Masonry Int 1997; 11(1):26-32.

[37] Pietruszczak S, Niu X. A mathematical description of macroscopic behavior of brick masonry. International Journal of Solids and Structures 1992; 29(5):531-546.
[38] Kawai T. New discrete models and their application to seismic response analysis of structures. Nucl. Eng. Des. 1978; 48: 207–229.
[39] Casolo S, Milani G. A simplified homogenization-discrete element model for the non-linear static analysis of masonry walls out-of-plane loaded. Engineering Structures 2010; 32: 2352-2366.
[40] Casolo S, Peña F. Rigid element model for in-plane dynamics of masonry walls considering hysteretic behaviour and damage. Earthquake Engineering & Structural Dynamics 2007; 36:1029–1048.
[41] Casolo S. Macroscale modelling of microstructure damage evolution by a rigid body and spring model. Journal of Mechanics of Materials and Structures 2009; 4(3): 551–570.
[42] Page AW. Finite element model for masonry. J Struct Div ASCE 1978; 104(8): 1267-85.
[43] Lourenço PB. Computational strategies for masonry structures. PhD Thesis. TU Delft, The Netherlands; 1996.
[44] Milani G. Simple homogenization model for the non-linear analysis of in-plane loaded masonry walls. Computers and Structures 2011; 89: 1586-1601.
[45] Raijmakers TMJ, Vermeltfoort A. Deformation controlled tests in masonry shear walls (in Dutch). Report B-92-1156, TNO-Bouw, Delft, The Netherlands, 1992.
[46] Lourenço PB, Rots J. A multi-surface interface model for the analysis of masonry structures. Journal of engineering mechanics 1997; 123(7): 660–668.
[47] Ganz HR, Thürlimann, B. Tests on masonry walls under normal and shear loading (in German). Report No. 7502-4, Institute of Structural Engineering, ETH Zurich, Zurich, Switzerland, 1984.
[48] Bertolesi E. Simple compatible homogenization strategies. Application to unreinforced masonry structures in and out of plane loaded. PhD Thesis, Department ABC, Technical University of Milan, Italy, 2016 (in preparation).